Mon. Not. R. Astron. Soc. **322**, 438–460 (2001)

The topology and polarization of sub-beams associated with the 'drifting' sub-pulse emission of pulsar B0943+10 – I. Analysis of Arecibo 430- and 111-MHz observations

Avinash A. Deshpande[1]★ and Joanna M. Rankin[2]★
[1]*Raman Research Institute, Bangalore 560 080, India*
[2]*Physics Department, University of Vermont, Burlington, VT 05405, USA*

Accepted 2000 October 3. Received 2000 October 2; in original form 1999 October 13

ABSTRACT

The 'drifting' sub-pulses exhibited by some radio pulsars have fascinated both observers and theorists for 30 years, and have been widely regarded as one of the most critical and potentially insightful aspects of their emission. Moreover, Ruderman & Sutherland, in their classic model, suggested that such regular modulation was produced by a system of sub-beams, rotating around the magnetic axis under the action of $\boldsymbol{E}\times\boldsymbol{B}$ drift. Such 'drift' sequences have thus been thoroughly studied in a number of pulsars, but it has proven difficult to verify the rotating sub-beam hypothesis, and thus to establish an illuminating connection between the phenomenon and the actual physics of the emission.

Here, we report on detailed studies of pulsar B0943+10, whose nearly coherent sequences of 'drifting' sub-pulses have permitted us to identify their origin as a system of sub-beams that appear to circulate around the magnetic axis of the star. We introduce several new techniques of analysis, and we find that both the primary and secondary features in the fluctuation spectra of the star are aliases of their actual values. We have also developed a method of tracing the underlying pattern responsible for the observed sequences, using a 'cartographic' transform and its inverse, permitting us to study the characteristics of the polar emission 'map' and to confirm that such a 'map' in turn represents the observed sequence. We apply these techniques to the study of three different Arecibo observations: a 1992 430-MHz sequence which includes a transition from the highly organized 'B' profile mode of the star to its disorganized 'Q' mode; a 1972 430-MHz 'B'-mode sequence; and a 1990 111-MHz 'B'-mode sequence.

The 'B'-mode sequences are consistent in revealing that the emission pattern consists of 20 sub-beams, which rotate around the magnetic axis in about 37 periods or 41 s. Even in the 'Q'-mode sequence, we find evidence of a compatible circulation time. The similarity of the sub-beam patterns at different radio frequencies strongly suggests that the radiation is produced within a set of columns, which extend from close to the stellar surface up through the emission region and reflect some manner of 'seeding' phenomenon at their base. The sub-beam emission is then tied neither to the stellar surface nor to the field. While the origin of the 'memory' responsible for the stability of the pattern over several circulation times is unknown, the hollow conical form of the average pattern is almost certainly the origin of the conal beam forms observed in most pulsars.

Key words: MHD – plasmas – polarization – radiation mechanisms: non-thermal – pulsars: general – pulsars: individual: B0943+10.

1 INTRODUCTION

We wish to reopen several questions that have lain dormant for the best part of 20 years. What is responsible for the spectacular sequences of 'drifting' sub-pulses observed in many pulsars with conal single (S_d) profiles? What are the topology and polarization of the individual beaming elements that correspond to these sub-pulses – and how do they accrue to form the average profile? How can we understand a range of other observed effects – profile and polarization modes, multiple P_3 values, 'absorption'

★ E-mail: desh@rri.ernet.in (AAD); rankin@physics.uvm.edu (JMR)

Table 1. Modulation feature frequencies.

Source	f_p(cycle P_1^{-1})	f_p alias	f_s(cycle P_1^{-1})	harmonic?
Taylor & Huguenin	0.477 ± 0.003	not cons'd	0.065 ± 0.005	no
Backer et al.	0.461 ± 0.010	not cons'd	0.078 ± 0.020	exact
Sieber & Oster	0.473 ± 0.002	0.527 ± 0.002	0.07 ± 0.01	not cons'd
1992/430 MHz	0.4645 ± 0.0003	0.5355 ± 0.0003	0.0710 ± 0.0007	exact
1972/430 MHz	0.4591 ± 0.0009	0.5409 ± 0.0009	not determined	–
1990/111 MHz	0.4688 ± 0.0005	0.5312 ± 0.0005	not determined	–

and sub-pulse 'memory' – in terms of fundamental emission processes and propagation effects within the pulsar magnetosphere?

From the initial identification of 'drifting' sub-pulses by Drake & Craft (1968), many suspected the phenomenon to be an unusually clear manifestation of the physical processes behind pulsar emission. Fluctuation-spectral analysis (taken over from scintillation studies) found its place almost immediately in assessing pulse sequences for periodicity (Lovelace & Craft 1968), and strenuous efforts were made by several groups to study the sub-pulse modulation in the then known stars (Taylor, Jura & Huguenin 1969; Lang 1969; Cole 1970; Sutton et al. 1970; Slee & Mulhall 1970). Backer's (1970a,b,c, 1971, 1973) thesis research carried these early efforts to understand 'drifting' sub-pulses to a new level; he systematized the then existing studies, clarified how sightline geometry could produce distinct modulation characteristics, developed the crucial technique of applying fluctuation-spectral analysis to each narrow longitude interval within the emission window (and of following the varying phase of a feature with longitude), and introduced the terms within which the 'drift' phenomenon is now almost universally understood.

Of course, the very existence of individual sub-pulses raises unresolved questions about how these distinct elements of emission are produced – but stars with periodic sub-pulse modulation ('drifting' in stars with single profiles and longitude-stationary modulation in those with double ones) have suggested, from near the time of their discovery, a system of regularly spaced sub-beams which rotate progressively around the magnetic axis of the star (Ruderman 1972). Several efforts have been made to delineate the beam topology and polarization characteristics of these sub-beams, but none has thus far been very successful. Pulsar B0809+74 has attracted special attention because its sub-pulse modulation is so remarkably regular (Sutton et al. 1970; Taylor & Huguenin 1971) – giving a strong, high-'Q' feature at some 0.090 cycle period^{-1} in its fluctuation spectra. However, the most creative efforts at measuring the polarization of its individual-pulse sequences have resulted in only marginal signal strength relative to the noise level (hereafter S/N), so that these characteristics are now known only in the average of several 'drift' sequences (Taylor et al. 1971).

Pulsar B0943+10 is another star in the same class as 0809+74. Its fluctuation spectra also exhibit narrow features – this time at about 0.47 cycle period^{-1} – but its unusually steep spectrum makes the star difficult to observe on a single-pulse basis at frequencies above 300 MHz. Its pulse-to-pulse modulation is then nearly odd–even, with alternate pulses appearing to progress slowly from the trailing to leading edge of the window over 15 or so periods. No entirely consistent picture has emerged from the existing studies of its 'drift' phenomenon. Taylor & Huguenin (1971) first associated the 'drift' pattern with another, weaker fluctuation feature at 0.065 cycle period^{-1} and attributed the stronger feature mentioned above to the nearly 'alternate pulse modulation'. Backer (1973) noted the general possibility that such a primary feature was an alias of the actual fluctuation frequency, but found no means of distinguishing between the possibilities. Backer, Rankin & Campbell (1975) then showed that the two features have an exact harmonicity if the secondary one is the aliased second harmonic of the primary one, but then went on to discuss the phase function of the primary feature without considering whether it also might be aliased. Finally, Sieber & Oster (1975) clearly discussed some of the aliasing possibilities, and attempted to distinguish between them, but (in our view) came to the wrong conclusion – and thus found no cause to mention any harmonicity between the features. We note that these various studies measured significantly different frequencies for the primary feature, which are summarized in Table 1.

PSR 0943+10 exhibits two distinct profile 'modes' at 102 MHz, designated 'B' and 'Q' by their discoverers, Suleymanova & Izvekova (1984). In an earlier paper (Suleymanova et al. 1998), the properties of these modal sequences were explored at 430 MHz for the first time using an exceptionally strong, 18-min polarimetric observation. The contrasting characteristics of the two modes are striking. The 'B' (for 'bright') mode entails a steady, highly organized pattern of sub-pulse emission – the 'drifting' sub-pulses discussed above – which is confined to the early part of the emission window; whereas the weaker 'Q' (for 'quiescent') mode produces disorganized, but occasionally much more intense, sub-pulses throughout the entire window. The primary and secondary polarization modes (PPM and SPM, respectively) are emitted in both 'B'- and 'Q'-mode sequences, the former well dominated by the PPM and the latter only slightly dominated by the SPM, respectively – resulting in different levels of aggregate linear depolarization.

These circumstances raise many questions about how the average, polarized modal profiles of the pulsar are composed of their respective pulse sequences, which were only partially addressed in the earlier paper. Furthermore, these sub-pulses directly reflect the electrodynamic processes responsible for pulsar emission – that is (according to the received 'cartoon'), primary particle acceleration associated with local 'sparking' regions near the polar cap, which in turn generate the secondary-plasma 'bunches' that radiate coherent radio emission. Therefore we will attempt to relate our observations and analysis to the general picture elaborated by Ruderman & Sutherland (1975).

Finally, something is known about the overall emission geometry of 0943+10. Estimates of its magnetic latitude angle α and impact angle β were made by one of us (Rankin 1993a,b) on the basis of the best information then available. It was clear even from these initial values that our sightline barely grazes the emission cone of the pulsar, reconfirming its classification as having a conal single (S_d) profile geometry. Moreover, at 400 MHz and above, the decreasing conal beam radius of the pulsar is apparently responsible for its extremely steep spectral decline (Comella 1971). Only recently have weak detections been reported at frequencies above 600 MHz [Deshpande,

Ramachandran & Radhakrishnan (private communication) at 840 MHz and Weisberg et al. (1999) at 21 cm]. At and below 100 MHz the pulsar is one of the brightest in the sky; indeed, to our knowledge it is the first and still the only pulsar discovered at a frequency below 300 MHz (Vitkevich, Alexseev & Zhuravlev 1969) – apart from the four original Cambridge pulsars – and it is unique in exhibiting no spectral turnover down to some 25 MHz (Izvekova et al. 1981; Deshpande & Radhakrishnan 1992).[1] Section 2 discusses our observations, and Sections 3–5 the modulation features and aliasing of the star. Section 6 assesses the emission geometry of the star. Section 7 discusses our sub-beam imaging technique and applies it to the 1992 'B'-mode sequence. The 'Q'-mode sequence is discussed in Section 8, while Section 9 covers the polarization-mode structure of the 'B'-mode sequence. Sections 10–11 discuss the older (1972) 430-MHz sequence and a more recent (1990) 111.5-MHz one. Finally, Section 12 briefly summarizes the arguments and conclusions.[2]

2 OBSERVATIONS

The single-pulse observations used in our analysis below come from two programmes carried out at the Arecibo Observatory over a long period of time. The newer 430-MHz observation was made on 1992 October 19 and is identical to that considered in an earlier paper by Suleymanova et al. (1998). Use of a 10-MHz bandwidth, across which 32 channels were synthesized by the 40-MHz Correlator, and a 1006-μs dump time reduced dispersion delay across the bandpass to negligible levels. The resolution was then essentially the dump time of $0\overset{\circ}{.}328$ longitude. The observational procedures will be described in a forthcoming paper (Rankin, Rathnasree & Xilouris, in preparation).

The older 430-MHz observation was carried out on 1972 January 2 with a single-channel polarimeter of 2-MHz bandwidth and 1-ms integration time, giving a nominal time resolution of about $1\overset{\circ}{.}1$ longitude. It is identical to that considered by Backer et al. (1975).

The 111.5-MHz observation was made on 1990 January 17 in an earlier phase of the 40-MHz Correlator based polarimetry programme. Use of a 2.5-MHz bandwidth and retention of 64 lags (channels) along with a 1406-μs dump time resulted in an effective resolution of about $1\overset{\circ}{.}265$. No continuum source observation was available to calibrate Stokes parameter *V* for this observation, so the baseline levels, which were dominated by galactic background noise, were thus used to calibrate the relative gains of the channels.

3 PRIMARY FLUCTUATION FEATURES

We first compute nominal 256-point fluctuation spectra for the 'B' mode of 0943+10, using the 816-pulse sequence (hereafter PS) at 430 MHz discussed by Suleymanova et al. (1998), and the result is shown in Fig. 1. The slow (about 30 per cent) intensity decrease over this interval (which they noted) was flattened before computing the spectra to avoid possible smearing of the otherwise high-Q ($=f/\Delta f$) features. As expected, these longitude-resolved fluctuation (LRF) spectra show a strong feature near 0.46 cycles per rotation period (hereafter cycle P_1^{-1}), which most fully

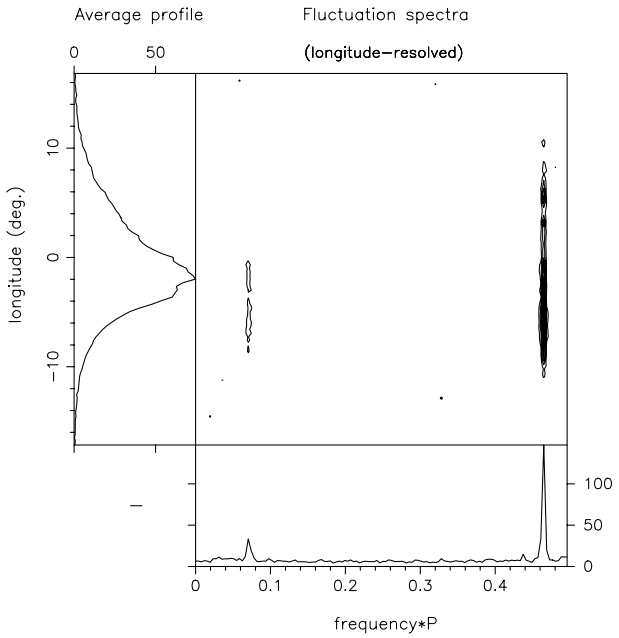

Figure 1. Longitude-resolved fluctuation spectrum for pulsar 0943+10 at 430 MHz. A 256-point FFT was used and averaged over the first 816 pulses of the 1992 October 19 observation. The body of the figure gives the amplitude of the features, with contours at intervals of 0.012 mJy^2, which reach a maximum value of 0.11 mJy^2. The average profile (Stokes parameter *I*) is plotted in the left-hand panel, and the integral spectrum is given at the bottom of the figure. The pulse-sequence amplitude was adjusted before analysis to remove the slow secular decrease [which is intrinsic to the pulsar: see Suleymanova et al. (1998)], so that any small 1/*f* 'tail' in the spectrum has been suppressed. Note that four distinct features are clearly visible in the integral spectrum, the two major features as well as a pair of weak features on either side of the principal one (see text).

modulates the power on the leading edge of the profile, but the effect of which can be discerned throughout the pulse window. The remarkable strength and narrowness of this feature are evident in the integral spectrum, from which its frequency can be accurately determined as 0.465 ± 0.001 cycle P_1^{-1}. This value agrees well with that measured by Backer et al. (1975), but is incompatible with those of Taylor & Huguenin (1971) and Sieber & Oster (1975) (which, paradoxically, are more accurate and consistent with each other); see Table 1. The half-width of the integral feature is less than 0.002 cycle P_1^{-1}, making its Q more than 200! No known pulsar, including 0809+74, has such a remarkably stable modulation feature.

None the less, the principal feature in Fig. 1 is not resolved with a Fourier transform of length 256. Longer fast Fourier transforms (FFTs) yield a progressively narrower feature, and even for a transform of length 816, the principal feature is only partly resolved. On this basis, we obtain an f_3 value of 0.4645 ± 0.0003 cycle P_1^{-1}, which implies a value of Q greater than 500. Sub-pulse modulation with such remarkable stability is unprecedented. Indeed, we cannot yet say whether this behaviour is typical or unusual even for 0943+10, but during this 14.9-min 'B'-mode sequence its sub-pulse modulation has a bell-like quality – and we see in Fig. 2 that the sequence is undisturbed by even a single null pulse.

A second feature is seen near 0.07 cycle P_1^{-1}, and it modulates the emission early in the 'B'-mode profile just as did the primary feature above. We calculate the frequency of this smaller feature

[1] Malofeev (private communication) now has evidence suggesting that the spectrum of the pulsar begins to turn over between 34 and 25 MHz.

[2] Some early results of this work appeared in Deshpande & Rankin (1999), Deshpande (1999) and Rankin & Deshpande (1999).

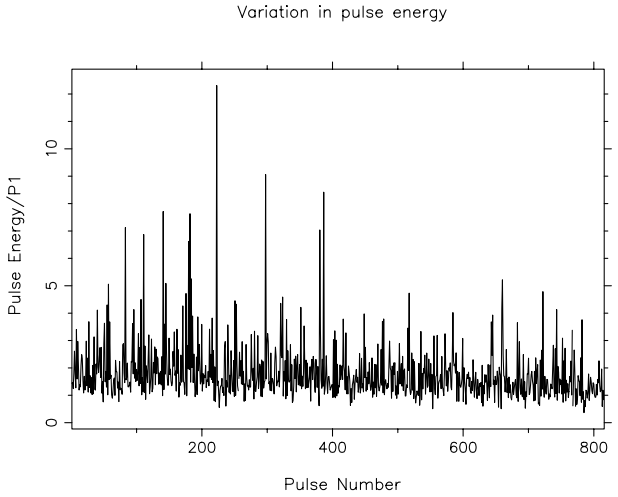

Figure 2. Pulse energy as a function of pulse number for the 816 pulses comprising the 'B'-mode sequence. Notice the slight secular decrease in intensity and its periodic tendencies, and, most of all, notice that there is not a single 'null' pulse!

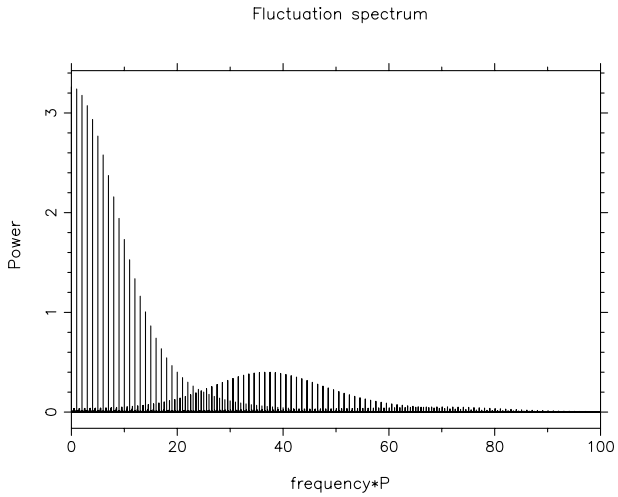

Figure 3. An unfolded fluctuation spectrum, obtained by continuously sampling the same sequence as in Fig. 1. Three successive, overlapping, 256-pulse Fourier transforms (each of length about 2.8×10^5 points, when the unsampled intrapulse region was interpolated with zeros) were averaged together. There are three main contributions to this diagram: (i) Harmonics at integral multiples of the fundamental $1/P_1$ pulsar-rotation frequency, which are related to the Fourier components of the 'average' profile. These are strongest at low harmonic numbers and have declined to a relative amplitude of 1/e by about number 15. (ii) Components falling at about half-integral frequencies $[(N + 0.535)/P_1]$, which peak at about harmonic 35. (iii) A set of components at frequencies near (but not exactly at) harmonics of $1/P_1$ $[(N + 0.071)/P_1]$, which peak near number 70. The latter two sets of components represent the harmonics of the highly periodic fluctuations associated with the sub-pulse modulation of the pulsar.

as 0.0710 ± 0.0007 cycle P_1^{-1}. We note also that the width of this feature is larger, about twice that of the principal one. An FFT of length 512 yields the slightly improved (mean) value of 0.0697 ± 0.0005 cycle P_1^{-1} – and clearly resolves the width of the feature.

The possible relationship between the two spectral features warrants detailed discussion. Of course, it is possible to speculate, as did Sieber & Oster (1975), that one or both of the features are aliases of fluctuations with frequencies greater than 0.5 cycle P_1^{-1}. Indeed, we can then confirm that, if the principal feature were the first-order alias ($1 - f_3 = 0.4645 \pm 0.0003$ cycle P_1^{-1}) of a fluctuation with an actual frequency f_3 of 0.5355 ± 0.0003 cycle P_1^{-1}, then its second harmonic $f_3' = 2f_3$ would fall at 1.0710 ± 0.0006 cycle P_1^{-1}; and this fluctuation would then have a second-order alias [f_3'(alias) $= f_3' - 1$] at 0.0710 ± 0.0007 cycle P_1^{-1}. If, however, the secondary feature appears as a first-order alias, the two might still have an harmonic relationship, because f_3' would be 0.9290 ± 0.0006 cycle P_1^{-1}, which would then have a first-order alias ($1 - f_3'$) of 0.0710 ± 0.0007 cycle P_1^{-1}. The measured frequencies accurately support the premise of an harmonic relationship as long as one or both are aliased as above; or, as Backer et al. concluded, it was 'possible to avoid the conclusion of an harmonic relationship only by assuming that the relationship is fortuitous'. In fact, even higher order aliases in suitable combinations would be consistent with the premise of an harmonic relationship. Therefore we can be certain about the harmonicity of the two features only if we establish their alias orders or – equivalently – their 'true' frequencies, a desired piece of information in any case.

In order to do so, we need to sample the fluctuations faster than just once a period. This may be possible by appealing to the fact that the fluctuations are sampled also within the finite width of the pulse. In other words, the fluctuation spectra at different longitudes can be combined appropriately based on their longitude separations to 'unfold' the contributions that are otherwise aliased within the 0–0.5 cycle P_1^{-1} band. In practice, we can achieve this simply by Fourier transforming the entire time sequence, which can be reconstructed using the available pulse sequence and filling the unsampled (off-pulse) regions with zeros. Such (power) spectra can be computed for pulse sequences in suitable blocks and then averaged. Care must be taken to ensure that the sampled region is wide enough to include the entire pulse-emission window (i.e. untruncated) and that the 'baseline' is removed correctly, so that the spectral features corresponding to the pulsar signal are not distorted. This effective windowing of the time sequence, where only the off-pulse contributions are forced to zero, leads to a convolution of the spectrum of the raw (unwindowed) time sequence with the spectrum of the periodic windowing function. However, it is easy to show that this convolution does not modify the spectral contribution of the pulsar signal, smoothing only the noise and hence, in fact, enhancing the signal-to-noise ratio (S/N) of the spectral features of interest.

The results of such a computation are given in Fig. 3, where only one half of the symmetric power spectrum is plotted as a function of frequency, normalized to the pulsar rotation frequency P_1. There is much to see in this diagram. First, note the amplitude of the frequency components at integral multiples of the pulsar rotation frequency. These are the Fourier components of its 'average' profile, which include contributions from its 'base' profile – or what is unchanging from pulse to pulse – as well as from its fluctuations seen on an average. The harmonics decline monotonically to a 1/e amplitude by about harmonic number 15; note that this corresponds approximately to the longitude width of the profile of 0943+10. Now notice the spectral components at about half-integral frequencies (actually $N + 0.535$ cycle P_1^{-1}), which grow steadily and peak around harmonic number 35 – a scale which corresponds approximately to the width of the individual 'drifting' sub-pulses, and more directly to P_2, the longitude separation between adjacent sub-pulses. Finally, notice the near-integral frequency components (actually $N + 0.071$ cycle P_1^{-1}) which begin to be distinguishable from the precisely integral

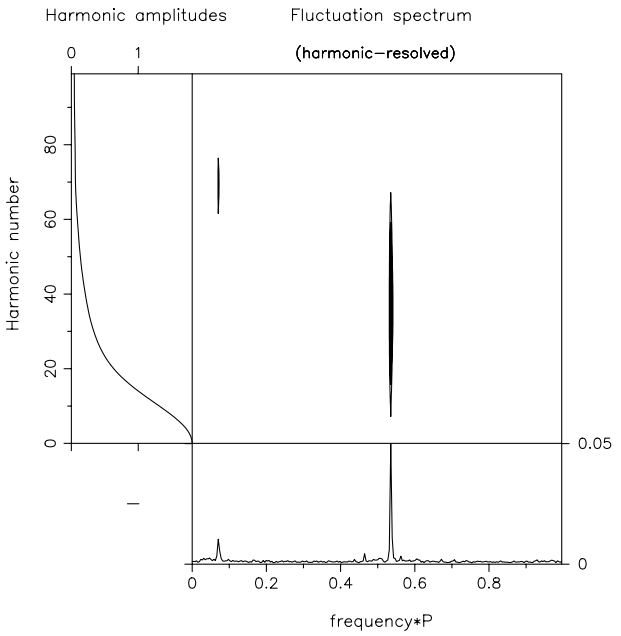

Figure 4. An unfolded Fourier spectrum as in Fig. 3. The amplitude of the frequency components at the fundamental rotation frequency $1/P_1$ and its harmonics are essentially the Fourier components of the 'average' profile; these are plotted in the left-hand panel of the diagram. The body of the figure gives the amplitude of all the other frequency components in the spectrum up to $100/P_1$ as a contour plot (with contours at amplitude intervals of $0.040\,\mathrm{mJy}^2$ which reach a maximum value of $0.353\,\mathrm{mJy}^2$), and the bottom panel shows the sum of these frequency components, collapsed on to a $1/P_1$ interval. The principal feature now falls at its true (unaliased; see text) frequency of about $0.535\,\mathrm{cycle\,period}^{-1}$ with its first harmonic at about $1.071\,\mathrm{cycle\,period}^{-1}$. We also see two 'sidelobes' associated with the principal feature, as well as a slight 'leak-through' at its alias frequency (from the unplotted negative-frequency portion of the spectrum).

components at harmonic numbers above 50 and which peak at about harmonic 70; these represent the Fourier components of the secondary feature. The relationship (i.e. the relative amplitude and phase) between these sets of modulation components defines the average 'shape' of the 'drifting' sub-pulses, while that among the components within a set defines the 'envelope' followed by the sub-pulse as it 'drifts' in longitude.

Just to make things clearer, we present the fluctuation spectrum of Fig. 3 in a different manner by stacking successive sections of $1/P_1$ width one above the other as shown in Fig. 4. We see immediately that the principal feature now falls at a frequency of about $0.535\,\mathrm{cycle}\ P_1^{-1}$. The power at a frequency of $1/P_1$ and its harmonics – which comprise the 'average' profile of the pulsar – are shown in the left-hand panel. The fluctuation power at other frequencies, as a function of $1/P_1$-frequency interval, is shown in the body of the figure, and the integral of this fluctuation power, summed into a single $1/P_1$ band, is given in the bottom panel. This spectral representation, which we will refer to as an 'harmonic-resolved fluctuation spectrum' (hereafter HRF spectrum), can also distinguish between the two types of modulation encountered, namely amplitude modulation and phase modulation. For example, the summed spectrum (as in the bottom panel) would exhibit nearly symmetrical modulation sidebands in the case of amplitude modulation, while a clear asymmetry would be apparent for phase modulation, as is presently the case.[3] So, although the two modulation types are in general mixed, the asymmetry between the 0.535 and $0.465\,\mathrm{cycle}\ P_1^{-1}$ features in Fig. 4 is so great that we can regard them as the signature of an almost 'pure' phase modulation.

Fig. 3 presents *exactly* the same information as in Fig. 4, but in a slightly more direct way. Note that nothing has been suppressed here. Both figures give the amplitudes of all the Fourier components of the PS, and this power falls predominantly in one of the three sets of components discussed above. Remarkably, the aggregate power in the non-integral components is comparable to that in the integral ones. The Fourier components of the noise are not discernible in either Fig. 3 or Fig. 4, implying that its power (as expected) is distributed uniformly over fluctuation frequency and is thus completely negligible in any given frequency interval.[4] Again, Fig. 3 clearly demonstrates the 'bell-like' quality of this 'B'-mode sequence from pulsar 0943+10.

We can now be certain that the principal feature in Fig. 1 is the alias of a fluctuation the actual frequency of which is greater than $0.5\,\mathrm{cycle}\ P_1^{-1}$ and that the secondary feature is its second harmonic. From Figs 3 and 4, it is clear that these features, seen in the LRF spectra, are indeed higher order aliases of the two sets of frequency components whose distances from zero frequency are harmonically related – that is, with maximum intensities at about harmonics 35 and 70, respectively. Using a 512-point FFT and interpolating the peak positions, we determine that the two responses have frequencies f_3 of $0.5352 \pm 0.0006\,\mathrm{cycle}\ P_1^{-1}$ and f_3' of $(1+)\ 0.0710 \pm 0.0006\,\mathrm{cycle}\ P_1^{-1}$ – accurately demonstrating their harmonic relationship. Further, we see that the secondary feature has a well-resolved width of about $0.0006\,\mathrm{cycle\,period}^{-1}$, more than twice that of the primary periodicity. Finally, given the strength and narrowness of the second harmonic of the primary feature, it is not ridiculous to explore the possibility of detecting its third harmonic, and a quick calculation $[f_3''(\mathrm{alias}) = 3f_3 - 1]$ confirms that it would fall at some $0.6065 \pm 0.0012\,\mathrm{cycle}\ P_1^{-1}$, where, indeed, a minor feature can be seen in Fig. 4.

One other line of evidence can be brought to bear on the aliasing of the observed features – that is, the fluctuation phase rate as a function of longitude associated with each of them. Their respective phase rates can be used to assess the harmonicity of the features, as well as to determine the 'drift'-band spacing (P_2) in longitude. Fig. 5 gives average profiles showing both the amplitude and the phase of the power associated with the primary and secondary features. The maximum rate in the former is just less than 36° per degree near the longitude origin, which is compatible with a longitude interval between sub-pulses P_2 of just over 10° – say, 10°.5. Note that the phase rate is less steep under the 'wings' of the profile, as might be expected if the sub-pulses move along a curved path. The phase rate of the secondary feature

[3] Were, for instance, our sightline to make a central traverse across the conical beam of 0943+10, rather than the highly tangential one that it does, we would expect to see the same primary modulation feature. However, it would appear as a longitude-stationary modulation – that is, as an amplitude modulation without 'drift' – and its fluctuation power would thus be divided between positive- and negative-frequency features corresponding to 'drift' to the right and to the left. Such pairs of identical features at positive and negative frequencies reliably identify the presence of amplitude modulation.

[4] Figs 3 and 4 also exhibit the exceptional quality of the Arecibo 40-MHz Correlator based PS observations. Were the noise not virtually 'white' (e.g. no 'red' contributions from receiver gain variations) and free of periodic contributions (e.g. from 60-Hz contamination), their effects would stand out sharply in these diagrams.

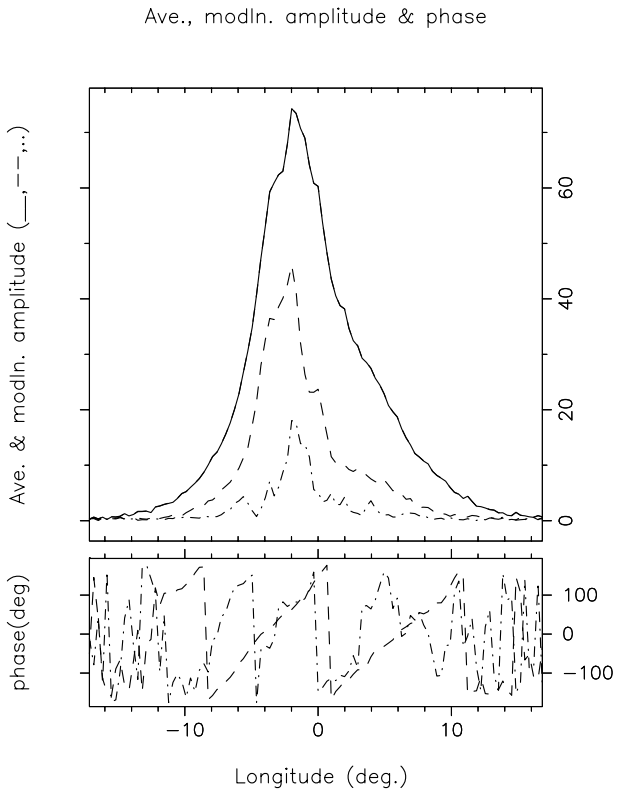

Figure 5. Fluctuation phase and amplitude for the primary (0.535 cycle P_1^{-1} – dashed curve) and secondary (1.070 cycle P_1^{-1} – dotted curve) features in Figs 3 and 4. The fluctuation power is plotted as a function of longitude within the average profile in the top panel, whereas the fluctuation phase is given in the lower panels.

is much faster and seems to reach some 70° per degree near the peak of the profile, where the fluctuation power also has a maximum. We have not reproduced here a similar figure for the ostensible third harmonic, which exhibits a phase rate nearly thrice times that of the primary feature. The harmonicity of these phase rates argues strongly that the 0.071 and 0.607 cycle P_1^{-1} features are, indeed, the aliases of the second and third harmonics of the primary feature *and* that we have correctly identified their alias orders. This conclusion is further corroborated by the fact that $1/P_2$(ms) is about N/P_1(ms), where N is the peak harmonic number (35) associated with the primary modulation feature.

In summary, the above analysis has assisted us in *unfolding* the otherwise multiply folded fluctuation spectrum of 0943+10 and ruling out various combinations of P_3 (along with their implied 'drift' directions). The ambiguity, however, between the remaining two possible combinations – namely, $P_3 < 2P_1$ (thus implying negative 'drift') and $P_3 > 2P_1$ (positive 'drift') – cannot be fully resolved through the above analysis, owing to the limited sampling of the modulation (which our sightline allows) during each rotation of the star.

4 SPACING OF THE ROTATING SUB-BEAMS

Given the regularity of sub-pulse 'drift' in the current 0943+10 sequence, and the implied stability of the 'drift' bands, an important geometrical issue can offer useful insight. If the stable sub-pulse 'drift' corresponds to a circular pattern of rotating sub-beams – as is envisioned by the received 'cartoon' of pulsar emission as well as by the Ruderman & Sutherland (1975) theory – then we should be able to estimate the angular (magnetic azimuthal) separation between the adjacent sub-beams using either (i) the observed longitude interval between sub-pulses (P_2), or (ii) the associated rotation in polarization angle (hereafter PA).[5] Of the two, we can use the PA rotation approach immediately – at least approximately.

We are then interested in the amount of PA traverse within an interval of longitude corresponding to the separation between sub-pulses – that is, P_2. If the sub-pulse 'drift' does correspond, in actuality, to a pattern of sub-pulse beams which pivot about the magnetic axis, then we might expect that the orientation of their linear polarization (which is ostensibly fixed to the projected magnetic field direction) will correspond closely to their magnetic azimuth.

Figs 6(a), (b), (d) and (e) give a composite of four average Stokes profiles corresponding to equal intervals of phase within the $1.87P_1$ primary modulation cycle. As expected, we see the average characteristics of two (or sometimes three) sub-pulses at progressively varying positions in longitude. These figures delineate the average polarization of the 'drift' sequence, and we will return to a fuller discussion of them below. However, note that the rotation of the PA over an interval corresponding to the spacing between the centres of these averaged sub-pulses (P_2) – what we call χ_{P_2} – is about $-28°$ when the sub-pulse pair straddles the longitude origin (or, in the 'drifting' profile, Fig. 6c). This immediately provides a direct means of estimating the number of sub-beams that are possibly arranged along a circular ring centred on the magnetic axis. Neglecting spherical effects and assuming that the sub-pulse beams fall closer to the magnetic than to the rotational axis, we find two possibilities: if $|\chi_{P_2}| > P_2(°)$, the magnetic azimuth interval between the sub-pulse beams η is $|\chi_{P_2}| - P_2$ and an inside (negative, poleward) sightline traverse is indicated, whereas, if $|\chi_{P_2}| < P_2$, then $\eta \sim |\chi_{P_2}| + P_2$ and the sightline makes an outside (positive, equatorward) traverse.[6] Here, $\eta \sim 28° - 10° \sim 18°$, and thus $360°/18°$ indicates about 20 sub-beams. A more precise determination of this number should be possible once the overall geometry has been determined, or on the basis of some other consideration (as we will see in the following section). It follows that the system of such sub-beams would make a full rotation around the magnetic axis in an interval of just 20 times P_3 – that is, a little less than 40 rotational periods of the star.

5 THE MODULATION ON THE MODULATION

Given the unprecedented stability of the phase modulation in the 0943+10 PS discussed above, we can legitimately attempt a level of analysis that would heretofore have been inconceivable. It is clear that any underlying pattern of rotating sub-beams is stable over many times the above $40P_1$ scale. This immediately implies that their number must be an integer. Also, we would expect to see a periodic feature corresponding to, in general, the rotational cycle of the sub-beam pattern unless all the sub-beams are identical (or utterly random) in amplitude. Such a tertiary periodicity, if any, would manifest itself as sidebands to the spectral features associated with the primary phase modulation. Whether such

[5] The sub-pulses of 0943+10 exhibit no distinct PA signature as reported for B0809+74 (Taylor et al. 1971) or B2303+30 (Gil 1992) – rather, the PA varies simply with the longitude and polarization mode.

[6] These approximations will be justified in Section 6.

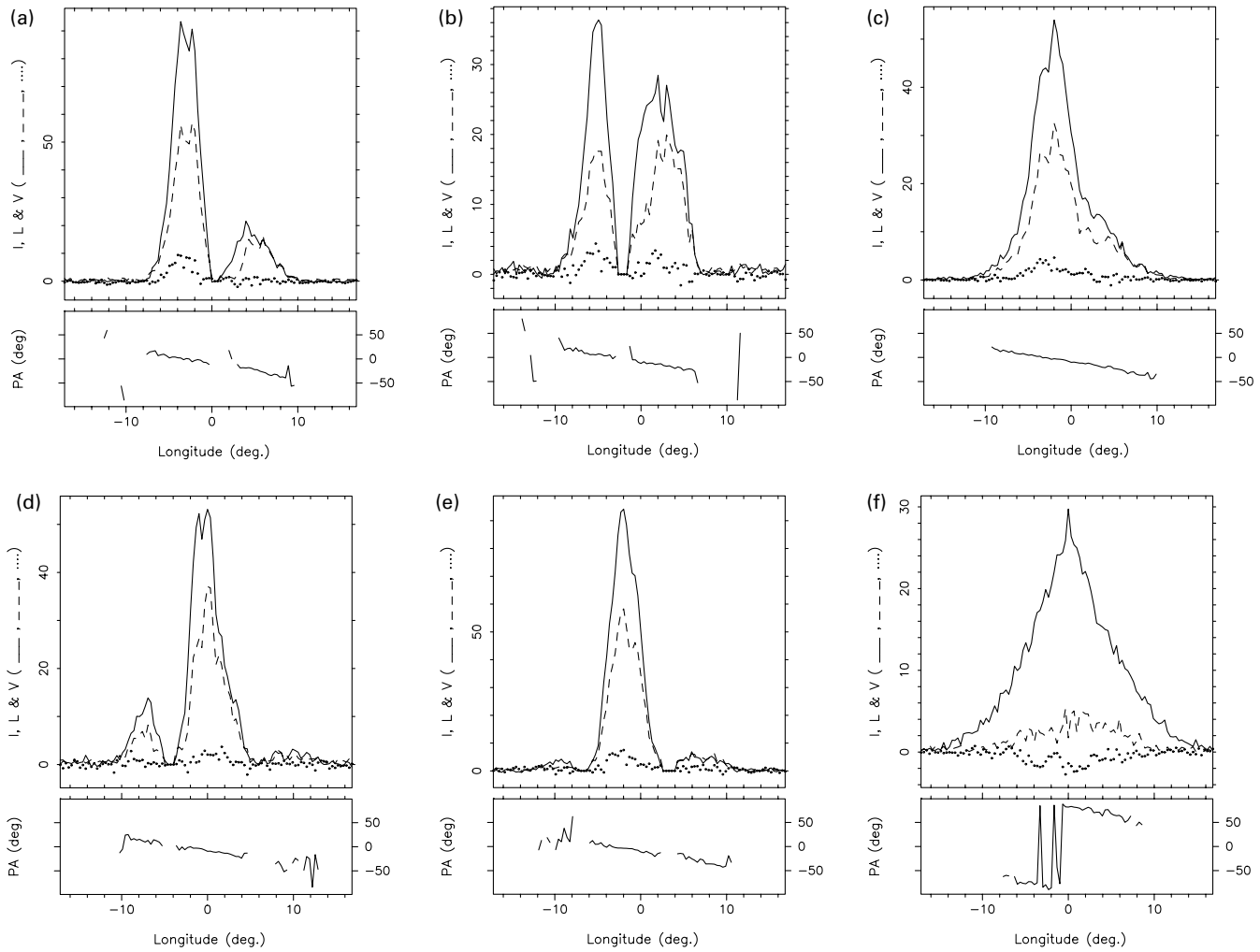

Figure 6. Composite of four partial polarization profiles (a, b, d, e) folded at different phases of the nominal $1.87P_1$ modulation cycle depicted in Fig. 8, as well as partial profiles of both the 'drifting' power (c) and the 'base' (f). All were computed from the entire 816-pulse 'B'-mode sequence of Fig. 1. Two and at times three sub-pulses are seen in the former which 'drift' progressively from later to earlier phases about 2°–3° from plot to plot. Note that the PA difference between sub-pulse peaks is negative and just less than 30° – a circumstance which is just compatible with 20 sub-pulse beams and an inside (poleward) sightline traverse (see text). This is very clearly seen in the PA behaviour of the 'drifting' (c) and 'base' (f) profiles, where we find PA rates of $-2\overset{\circ}{.}7$ and perhaps about $-3°$ per degree, respectively.

sidebands are symmetric or not would depend on whether the sub-beams differ from each other only in intensity, or in interbeam spacing or in both, and their narrowness would depend on how stable the sub-beam pattern is in time.

Two other minor features can be discerned in Figs 1 and 4 which fall symmetrically about the primary one, and their change of position in Fig. 4 shows that all three features are aliased responses in Fig. 1. These features are seen even more clearly in the spectra corresponding to a small part of the sequence (pulses 129–384) as shown in Fig. 7. Careful measurements (using the fluctuation spectra over only a few degrees of central longitude where the modulation sidebands are significantly stronger) indicate that these minor features fall at frequencies about $0.026\,80 \pm 0.000\,37$ cycle P_1^{-1} higher and lower than does the primary one at 0.535 cycle P_1^{-1}.

The separation of the minor feature pair from the primary is indicative of a major frequency component in the fluctuation power of the tertiary amplitude modulation. Lower frequency amplitude modulation would produce symmetrical features closer to the fundamental, and nothing is seen in the fluctuation spectra here. Consequently, that there is just one obvious such pair of 'simple' – that is unimodal – features associated with the tertiary amplitude modulation suggests that it is itself here tone-like. Were this tertiary modulation more complex, we would expect to see additional pairs of symmetrical features at larger (but harmonic) separations from the primary one, and only a slight deviation from the tone-like modulation is discernible in Fig. 7.

As already noted, the 'drifting' character of the pulse sequences of 0943+10 as well as the asymmetrical nature of the primary feature in its HRF spectrum are strongly indicative of a phase modulation. The *narrow* and *symmetrical* pair of features about the primary one in Fig. 7 (and also in Figs 1 and 4) strongly suggest the presence of a regular, highly periodic, amplitude modulation *of* the exquisitely regular phase modulation associated with the 'drifting' sub-pulse sequences of the star. This suggests that the putative sub-beams differ from each other primarily in their intensities, and that the intensity variations are a rather smooth and stable function of magnetic azimuth.

The period of this tertiary modulation is then some $(1/0.0268)P_1$ cycle^{-1} or just over $37P_1$ (i.e. $37.35 \pm 0.52P_1$).

Given that the length of the sequence analysed corresponds to many times this tertiary cycle and that the 'sidelobe' features have the sharpness suggestive of a remarkably stable modulation, a harmonic relationship between the two periods must exist. We note immediately that the tertiary modulation cycle is indeed very close to 20 times the period of the fundamental phase modulation, which at $(1/0.5355)P_1$ cycle^{-1} or some 1.867 rotation periods has a 20-cycle period of some 37.35 ± 0.03 rotation periods. This agreement is no accident or coincidence; any tertiary modulation not fully commensurate with the primary phase modulation would either broaden the primary feature or distort the 'sidelobes' around it. Given the accuracy to which the frequencies of the secondary and tertiary modulations can be estimated, we can now conclusively rule out the possibility that P_3 is greater than 2 rotation periods, because $(1/0.4645)P_1$ cycle^{-1} is simply not harmonically related to $37.35P_1$. The only commensurate value of P_3 (the one smaller than $2P_1$, as discussed earlier) implies with certainty that the 'drift' direction is *negative*. The observed harmonic relationship then also allows us now to adopt a refined estimate of the tertiary modulation period as simply 20 times the better determined value of P_3. It is important to emphasize here that, while the integral relationship between the modulation frequencies has resolved the longstanding 'drift' direction (aliasing) ambiguity, the exact number of sub-beams (20) is in no way crucial to our further analysis below.

Therefore we believe that this analysis has resolved the question of how and which way the sub-pulses of pulsar 0943+10 'drift'. Sieber & Oster's (1975) fig. 1 delineates some of the aliasing possibilities. Their 'A' band represents an apparent 'drift' with a P_3 of some 15, and it seems to entail gradual sub-pulse motion from later to earlier phases – that is, a *negative* 'drift'. Band 'B' ostensibly represents a negative 'drift' associated with a value of P_3 just less than 2, and band 'C' one with a P_3 just greater than 2.

Stated differently, Sieber & Oster's diagram clearly indicates the nearly alternate-pulse character of the basic modulation. It is therefore not straightforward to distinguish whether the basic 'drift' is to the right or to the left. Furthermore, as these authors emphasize, the LRF spectra in Fig. 1 – and all others like it – have the same difficulty. Any of the features in such a diagram can be aliases of fluctuations at frequencies greater than the 0.5 cycle P_1^{-1} Nyquist frequency associated with sampling at a $1/P_1$ rate. Only by appealing to the finite width of the pulse can this ambiguity be alleviated, as we have demonstrated above.

The 'B' track in Sieber & Oster's plot is then the fundamental oscillation associated with the 'drift' of 0943+10, and the 'A' track its first harmonic. This establishes the 'drift' direction as negative. The fundamental 0.535 cycle P_1^{-1} periodicity implies an associated P_3 value of some 1.867 periods – that is, in two rotations we see the *next* sub-pulse at a slightly earlier phase. Also, the effective 'P_3' of the second harmonic is $1/1.07$ or about $0.93P_1$ cycle^{-1} – the difference of which from $1.0P_1$ cycle^{-1} describes the 'A' track, while the conspicuously missing alternate sub-pulses are due to the fundamental modulation.

The basic character of this 'drift' behaviour can now be unambiguously represented by folding the entire 816-pulse 'B'-mode sequence at the $1.867P_1$ interval corresponding to the primary 0.535 cycle P_1^{-1} feature. We give such a display in Fig. 8, where the sub-pulse intensity as a function of longitude and phase within the modulation cycle is shown as a contour plot in the central panel. The varying energy in the modulation is given in the left-hand panel and the non-fluctuating 'base' (minimum-intensity) profile is shown in the bottom panel. While this display resolves longstanding questions about the 'drift' of pulsar

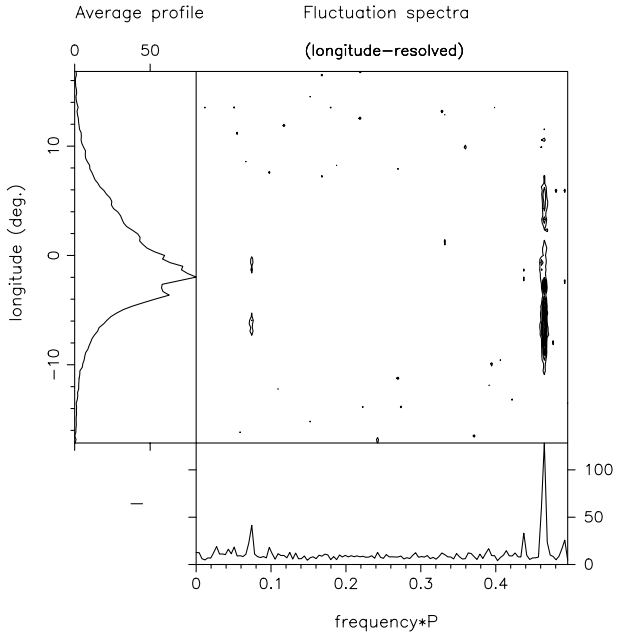

Figure 7. Fluctuation spectra as in Fig. 1 for pulses 129–384. The 'sidebands' of the principal feature are particularly strong in this subsequence (see text). The contour interval is 102 mJy^2 up to a maximum of 714 mJy^2.

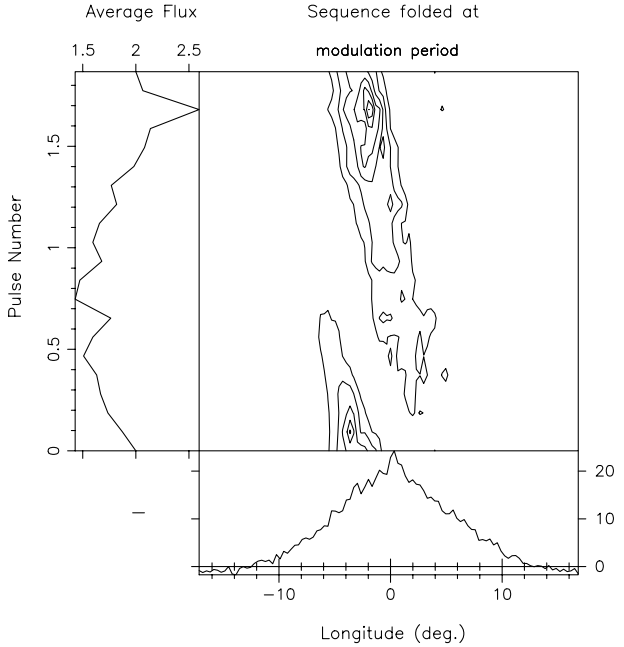

Figure 8. Block-averaged pulse sequence which corresponds to the principal 'drift' pattern in the 'B' mode of pulsar 0943+10. The 816 individual pulses are folded at the $1.867P_1$ interval, corresponding to the primary modulation feature (alias resolved) at some 0.5355 cycle P_1^{-1} in Fig. 2. The strength of the feature as a function of longitude and phase within the 1.87-period cycle is given as a contour plot in the body of the figure, and its integrated energy as a function of phase in the left-hand panel, whereas the aperiodically fluctuating 'base' (which has been removed from the other displays prior to plotting) is given in the bottom panel. Contours fall at about 26.7 mJy up to a maximum of 187 mJy.

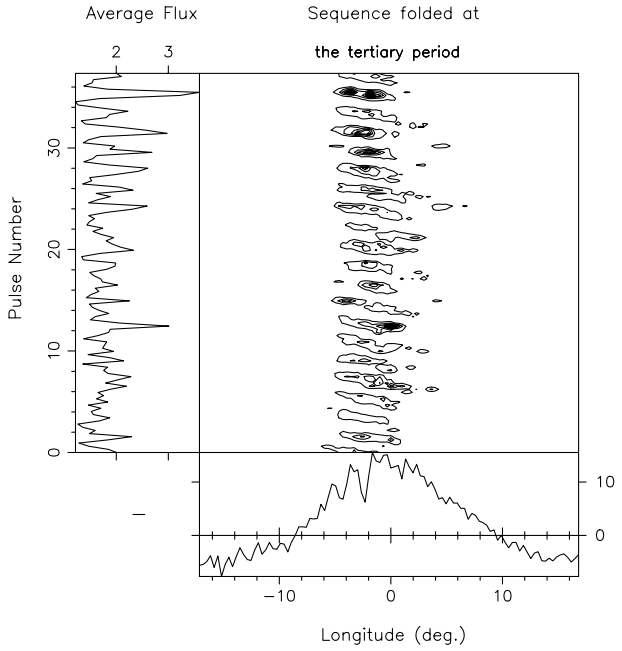

Figure 9. Block-averaged pulse sequence corresponding to the 430-MHz 'B'-mode observation in Figs 1–4. The 816 individual pulses are folded at the tertiary modulation period, which was calculated to be 37.346 rotation periods. Average pulse intensity as a function of longitude is represented in the body of the figure as a contour plot (contours at 51 mJy up to 457 mJy). The longitude-integrated intensity over the period of the tertiary-modulation cycle is plotted in the left-hand panel, and the amplitude of the aperiodically fluctuating 'base' – which is subtracted from the other displays – is given in the bottom panel.

0943+10, we now also see that its overall character is remarkably complex.

Finally, the conclusion that the 'drift' of pulsar 0943+10 is *negative* is very important to arguments that we will make in the following sections. The actual *physical* direction of the sub-pulse 'drift' *observed* is negative – that is, it is apparently in the *same* direction as the rotation of the pulsar.

Having established that the tertiary modulation cycle is 20 times the primary P_3 period of $1.867P_1$ cycle^{-1}, the interpretation is clear. We therefore conclude that the observed 'drifting' behaviour is a manifestation of the rotation of a relatively stable system of 20 sub-beams of systematically differing intensity, spaced uniformly in magnetic azimuth.

One means of verifying this circumstance is to fold the PS at the tertiary-modulation period, and it would be prudent to use the value based on the phase modulation, which we calculated above. The result for the 816-pulse sequence under consideration is shown in Fig. 9, and it bears detailed discussion. The average amplitude as a function of longitude over the tertiary-modulation cycle is depicted in the body of the figure; the integral over longitude is given at the left, and the amplitude of the aperiodically fluctuating 'base' (which has been subtracted before plotting the other panels) is shown in the bottom panel.[7]

[7] We note here that this 'base' profile [see also Fig. 6(f)] has a width of some 11°–12°. It is not at all clear what interpretation should be made of this 'steady' (as against the phase-modulated) contribution to the pulse sequence, but, were we to interpret this 'base' feature as a core component, it is interesting both that its form is symmetrical about the longitude origin (whereas the 'drifting' power is not at all so) and that its width is suggestive of a magnetic colatitude of some 11°–12° [Rankin 1990, equation (5)].

First, note the remarkable circumstance that folding at the tertiary-modulation period reveals an orderly subsequence of 20 replicating emission elements, each of which has its own distinct relative amplitude and behaviour as a function of longitude. As is expected, one of the 20 elements is significantly stronger than the others by upwards of a factor of 2. Although each extends over 6°–8° or more in longitude, some peak much earlier than others and exhibit a surprising range of individual characteristics: the brightest one, for instance, has a double amplitude structure. We emphasize that these elements *must* be relatively stable over this 15-min 'B'-mode sequence; it is their consistent brightness, and systematic variation in brightness, that apparently produces the amplitude modulation at a frequency 1/20th that of the primary phase modulation. We do not usually think of the processes associated with sub-pulse 'drift' as having stability on such long time-scales – and it is very possible that they usually do not.

None the less, given the regularity of sub-pulse 'drift' in the current 0943+10 sequence and the evidence that it entails a further modulation indicative of a repeating pattern of just 20 elements, we are forced to reconsider received ideas about the 'drifting sub-pulse phenomenon' and its possible origin in a pattern of slowly rotating sub-pulse beams (Ruderman & Sutherland 1975). Our results provide unexpectedly strong support for the simple 'cartoon' understanding of 'drifting' sub-pulses as a regular pattern of emission centres rotating around the magnetic axis of the pulsar.

6 THE EMISSION GEOMETRY OF PULSAR 0943+10

We expect a pulsar with *'drifting'* sub-pulses to have an emission geometry characterized by a highly tangential traverse through (or, perhaps better, along) one of the hollow conical beams associated with pulsar radiation. Uniquely for 0943+10, our sightline apparently grazes its beam so narrowly that we miss ever more of its emission at higher frequencies. The pulsar is thus an excellent example of the conal single (S_d) class (Rankin 1993b), and its value of B_{12}/P^2, which is about unity, supports this classification. Questions, none the less, remain about its geometry. Do we observe an inner or an outer cone (e.g. Rankin 1993a)? Does our sightline pass poleward or equatorward of the magnetic axis (e.g. Narayan & Vivekanand 1982)? Can we understand the steep spectrum of the pulsar in terms of the narrowing of the cone with frequency? Finally, is the overall conal geometry consistent with the 20-beam 'carousel' pattern indicated by the tertiary modulation?

Information on the geometry of the pulsar comes from considering its PA traverse in conjunction with its profile width. Then we can model these values using the relations in Rankin (1993a, equations 1–6). Reference to Suleymanova et al.'s fig. 4 – which treats the same 1992 430-MHz sequence – shows the PA behaviour for the 816 'B'-mode and 170 'Q'-mode pulses, and it is clear that the two modes exhibit somewhat different PA sweep rates. Their table 2 gives values of $-2\overset{\circ}{.}4$ and $-3\overset{\circ}{.}6$ per degree for the 'B'- and 'Q'-mode PA rates at 430 MHz, and $-3\overset{\circ}{.}4$ and $-3\overset{\circ}{.}6$ per degree at 102.5 MHz, respectively. Also important is their fig. 8, which shows the evolution of the 'B'- and 'Q'-mode profiles between 25 and 430 MHz. A further set of time-aligned profiles from Arecibo observations is given by Hankins, Rankin & Eilek (in preparation).

Our initial problem for 0943+10 is that we do not know where

we cross its 430-MHz beam – that is, where β (the impact angle of the sightline with respect to the magnetic axis) falls with respect to ρ (the outside, half-power radius of the conal emission beam). At higher frequencies our sightline cuts well outside the radial maximum and ultimately outside the half-power point ρ, whereas at lower frequencies the double-profile forms indicate cuts inside the radial maximum point. Therefore the observed dimensions of the 430-MHz profile will probably not correspond to those given for the overall pulsar population by Rankin (1993a) – even if we could extrapolate properly to 1 GHz – because those are based on more central sightline traverses that *do* cross the radial maximum point on the hollow conical emission beam.

Let us then model the 0943+10 geometry for each of four possible configurations (inside traverse, inner cone; inside traverse, outer cone; outside traverse, inner cone; and outside traverse, outer cone) as follows. (i) Calculate the conal beam radii ρ throughout the entire frequency range using Mitra & Deshpande's (1999) expression [patterned after Thorsett's (1991) profile width relation] with trial values of the index a as

$$\rho = \rho_{\mathrm{outer(inner)}}(1 + 0.066 f_{\mathrm{GHz}}^{-a}) P_1^{-1/2}/1.066, \quad (1)$$

where the 1-GHz values of the conal beam radii $\rho_{\mathrm{outer(inner)}}$ are taken according to Rankin's equation (5).[8] (ii) Least-squares fit the observed low-frequency profile widths (111.5 MHz and below) to calculated values from the usual spherical geometric relation

$$\Delta\psi = 4\sin^{-1}\left[\frac{\sin(\rho/2+\beta/2)\sin(\rho/2-\beta/2)}{\sin\alpha\sin(\alpha+\beta)}\right]^{1/2} \quad (2)$$

(Gil 1981; Rankin 1993a) with trial values of the magnetic colatitude α and sightline impact angle β. (iii) Least-squares fit the frequency-dependent part of equation (1) to obtain the index a, using it in step (i) above in an iterative solution. With this procedure, one is equipped to estimate the values of β/ρ even at frequencies where β exceeds ρ.

Two further useful quantities can be calculated here. One is the magnetic azimuth angle η that corresponds to a particular value of P_2. Using very simple spherical geometry, this angle is given (for small angles) by

$$\eta = 2\sin^{-1}[\sin(P_2/2)\sin(\alpha+\beta)/|\sin\beta|], \quad (3)$$

where P_2 is measured as a longitude interval (not a time), and for 0943+10 at 430 MHz has a value of just over 10°. Reference to Fig. 6 gives P_2 values in the 8.°5–9.°0 range, but a more accurate value comes from the fluctuation-spectral phase rate of the primary (0.535 cycle P_1^{-1}) feature in Fig. 5 – around 0° longitude the phase rate is some 34° ± 1° per degree, which implies a P_2 value of 10.°6 ± 0.°6. [The smaller values implied by Fig. 6 probably reflect the curvature of the sub-beam track relative to the sightline. Note that (see just below) $10.^\circ 6\cos\chi_{P_2} \approx 9^\circ$]. Clearly, if the 'drifting' represents a pattern of 20 sub-beams around the periphery of the polar cap, then this angle η must take a value of just 18°.

Another geometrical parameter associated with the 'drifting' pattern is the PA rotation between sub-pulses – what we called 'PA P_2' above. This PA rotation directly reflects the relative curvatures of the sightline and the conal beam. Its value is easily calculated from the usual single-vector model (Radhakrishnan & Cooke 1969; Komesaroff 1970) by evaluating $\chi_{P_2} = \chi(P_2/2) - \chi(-P_2/2)$, or

$$\chi_{P_2} = 2\tan^{-1}\left[\frac{\sin\alpha\sin(P_2/2)}{\sin(\alpha+\beta)\cos\alpha - \cos(\alpha+\beta)\sin\alpha\cos(P_2/2)}\right]. \quad (4)$$

Incidentally, equations (3) and (4) reduce nicely to rationalize the rules we used in Section 4. For small angles equation (4) reduces to $\chi_{P_2} \simeq R_{\mathrm{PA}} P_2$ (where the PA sweep rate $R_{\mathrm{PA}} = \sin\alpha/\sin\beta$), and equation (3) to $\eta \simeq (|R_{\mathrm{PA}}| + |\beta|/\beta)P_2$; thus $\eta \approx \chi_{P_2} + \mathrm{sgn}\beta P_2$ and will always be positive as long as the sub-beams fall closer to the magnetic axis than to the rotation axis.

Computations for all four emission geometry models were carried out to determine the best-fitting values of α, β and a, such that $\chi^2 = (1/3)\sum[(w - w_{\mathrm{c}})/\Delta w]^2$, where Δw was taken as 0.°4. The first of these models – our preferred one, for an inner traverse and inner cone – is given in Table 2. The columns giving ρ, β/ρ and the emission height h [from the centre of the star; see Rankin's (1993a) equation (6)] depend only on the fitted values of α, β and a. w and w_{c} are the respective measured (taken, wherever possible, in the 'B' mode for consistency) and modelled outside, half-power profile widths (the latter from equation 2). ρ_{c} (not shown) was computed for comparison from Rankin's equation (4), and the quantities R_{PA}, η and χ_{P_2} evaluated from the best-fitting parameters.

Table 2. Inner cone, inner traverse emission model.

f(GHz)	ρ(°)	β/ρ	h(km)	w(°)	w_{c}(°)
1.000	4.13	−1.04	125	–	–
0.430	4.23	−1.01	131	7?	–
0.306	4.29	−1.00	134	–	0.1
0.111	4.49	−0.96	147	16.5	16.7
0.103	4.51	−0.95	149	17.5	17.5
0.061	4.65	−0.92	158	23	22.7
0.049	4.72	−0.91	163	25	24.8
0.040	4.79	−0.89	168	27	26.9
0.034	4.85	−0.88	172	28	28.6
0.025	4.98	−0.86	181	32	31.8

Notes. Observational constants: P_2, 10.°5. Fitted parameters: α, 11.°58; β, −4.29; a, 0.396; χ^2, 1.12. Derived parameters: R_{PA}, −2.°7 per degree; η, 18.°0; χ_{P_2}, −27.°9.

A quick scan of Table 2 shows immediately that the inner cone, inner traverse model yields an excellent fit and reasonable parameters. This is also true for the outer cone, inner traverse model which gives almost identical results, but with $\alpha = 15.^\circ 39$ and $\beta = -5.^\circ 69$. The two models have virtually identical values of β/ρ, R_{PA}, η, χ_{P_2} and χ^2, so the fitting does not distinguish between them; indeed, models with any reasonable 1-GHz ρ-value would appear to behave similarly.

By contrast, the outer traverse models are of two different types. Inner and outer cone models with values of α and $|\beta|$ similar to those above have nearly identical values of R_{PA} and χ_{P_2} (and a about 0.53), but yield slightly poorer fits ($\chi^2 \sim 2.2$). These, however, result in very different values of η – about 42° – as might have been expected from equation (3), which depends strongly on the *sign* of β, unlike virtually all other geometrical

[8] While most pulsars exhibit what Rankin (1993a,b) defined as 'inner' and 'outer' cones, there is now evidence that a few stars exhibit cones with both larger and smaller characteristic radii (Gil, Kijak & Seiradakis 1993; Kramer et al. 1994; Rankin & Rathnasree 1997; Mitra & Deshpande 1999).

relations [i.e. equation (2) or (4)]. Finally, there are a pair of inner and outer cone 'pole in cone' models with α-values of about $2\overset{\circ}{.}9$ and $4\overset{\circ}{.}0$, respectively, and $R_{\rm PA} = 0.7$, $\eta = 18^\circ$, a χ_{P_2} of about $+7\overset{\circ}{.}4$, and a χ^2 of about 1.6. Clearly, none of these models is acceptable because the former fail to match the observed values of η and the latter fail to match those of $R_{\rm PA}$ and χ_{P_2}.

Our slightly circuitous means of computing the geometry of pulsar 0943+10 – using only profiles at 111 MHz and below, where the resolved double forms show that $|\beta|/\rho$ is well less than unity – permits us to assess how the sightline cuts the beam of the pulsar at higher frequencies. The row in Table 2 just above 111 MHz gives the frequency for which $w_{\rm c}$ is near zero – that is, the frequency at which the model ρ would be equal to $|\beta|$. At 430 MHz, the table shows that our sightline passes just outside the half-power radius on the conal beam, by $0\overset{\circ}{.}07$ and $0\overset{\circ}{.}09$, or some 1.5 per cent according to the two inner traverse models, respectively. No wonder that 0943+10 is so difficult to detect at frequencies above 400 MHz!

We can now draw some remarkable conclusions. We noted in Section 3 that the sub-pulse 'drift' of 0943+10 is negative – that is, in the same direction as its rotation. Then we concluded just above that our sightline makes an inside (negative) traverse – that is, crossing between the magnetic and rotational axes, with a negative rotation of the PA. If we imagine that we are looking at the pulsar with the 'closer' rotational pole 'up', then the emission beams must sweep past our sightline from right to left, thus implying that, from our perspective, the pulsar is rotating clockwise.[9]

Further, the sub-pulse beams are also rotating from right to left, but around the magnetic axis, which is 'below' us; therefore, they rotate around the polar cap counterclockwise (in the frame of the star). This 'drift' in 0943+10 is opposite to the Ruderman & Sutherland (1975) sense (see their fig. 4); they discuss Ferraro's Theorem in an appendix but do not clearly state its implication that polar cap plasma must rotate in the same direction as the star as viewed by an inertial observer. Ruderman (1976) then gives a correct and clear discussion of this point.

7 IMAGING THE EMISSION ZONE

The remarkable order implied by Fig. 9 of just 20 sub-pulse emission beams rotating about the magnetic axis of the star demands a further level of analysis. We have therefore developed a coordinate transformation between the usual system of pulsar (rotational) colatitude ζ ($= \alpha + \beta$) and longitude φ and a system rotating about the magnetic axis described by colatitude R and azimuth Θ. The emission beams rotate around the pole with the period of the tertiary modulation, which is here also $\hat{P}_3 = NP_3$, where (just as in Ruderman & Sutherland 1975) N is the number of sub-beams and P_3 the (unaliased!) sub-pulse 'drift' interval.

If, further, we number the pulses by k from a reference pulse k_0 and measure the longitude φ relative to an origin defined by that of the magnetic axis φ_0, then Θ is the sum of a rotation $\theta_{\rm rot}$ and a transformation $\theta_{\rm trans}$ as follows:

$$\Theta = A\,\theta_{\rm rot} + B\,\theta_{\rm trans}, \tag{5}$$

[9] Our discussion here is not fully consistent with the conventions of the rotating-vector model (RVM), which are reviewed nicely by Everett & Weisberg (2000). In our case, the 'closer' rotational pole points away from the direction of the angular momentum vector of the star, so that $\alpha_{\rm RVM}$ is $180^\circ - \alpha$, and $\beta_{\rm RVM}$ is $-\beta$.

where A and B can be either $+1$ or -1, defining the signs of the two contributions above. The sign of B is simply equal to that of the PA sweep rate observed, whereas the sign of A depends on the observed 'drift' direction as well. The sign constant A is -1 (i.e. negative) when the *true* sense of 'drift' and that of the observed (apparent) PA traverse match; otherwise it is positive. It is clear that, for B0943+10, the sign of A should be negative. It is worth mentioning here that this is consistent with what would be expected according to Ferraro's theorem (e.g. Ferraro & Plumpton 1966). Interestingly, the signs of both A and B do not seem to depend in any explicit way on the sign of β. However, as is well known, the sense of apparent PA traverse and the sign of β together determine the sense of rotation of the star with respect to the pole nearest to our sightline. When the sign of β matches the sense of PA traverse, the stellar rotation is clockwise; otherwise it is counter-clockwise.

The two quantities, $\theta_{\rm rot}$ and $\theta_{\rm trans}$, are given by

$$\theta_{\rm rot} = 2\pi[k - k_0 + (\varphi - \varphi_0)/2\pi]/\hat{P}_3, \tag{6}$$

$$\theta_{\rm trans} = \sin^{-1}[\sin\zeta \sin(\varphi - \varphi_0)/\sin R], \tag{7}$$

where

$$R = 2\sin^{-1}[\sin^2(\varphi/2 - \varphi_0/2)\sin\alpha\sin\zeta + \sin^2\beta/2]^{1/2}. \tag{8}$$

Correct identification of the longitude of the magnetic axis φ_0 is very important for carrying out the above transformation. Usually, the magnetic axis is expected to fall close to the centre of a profile, but, for 0943+10 at 430 MHz, Suleymanova et al. (1998) have shown that the 'B'-mode profile is truncated on its trailing edge, compared with its 'Q'-mode counterpart. It is, however, only the 'B'-mode profile that is truncated at 430 MHz; the 'Q'-mode profile is much broader. If we take the centre of the latter as close to the magnetic axis, note that this point falls close to the trailing half-power point of the 430-MHz, 'B'-mode profile (see Suleymanova et al. 1998, figs 4 and 8). [The inflection point of the PA traverse should lie close to the magnetic axis (apart from small relativistic effects: Blaskiewicz, Cordes & Wasserman 1991), but that point is difficult to determine accurately for this pulsar.] Finally, we can appeal to the time-aligned average profiles in Hankins et al. (in preparation). Note that some of the 430-MHz profiles are narrow and early (and thus presumably 'B'-mode-dominated); whereas another one is more extended and appears to be primarily a 'Q'-mode average. Overall, we see here that the point on the 430-MHz, 'B'-mode profiles that aligns best with the centres of their low-frequency counterparts is the half-power point on their trailing edge. We will then take this point, provisionally, as our best estimate of the longitude of the magnetic axis. Note that this choice results in the highly symmetrical 'base' profiles in Figs 6, 8, 9 and 18 (see later); see also footnote 7.

With all the necessary ingredients at hand, we proceed to perform the 'cartographic' transform defined by the above equations (and the inside traverse, inner cone model in Table 2) and thus to *reconstruct* an image of the accessible emission zone, based on the *observed* 'B'-mode sequence of 816 pulses. The result is given in Fig. 10, with the emission-pattern image or 'map' projected on to the polar cap shown in the main panel. The bottom and the side panels show the average- and the 'base'-intensity profiles, respectively, as functions of the angular distance from the magnetic axis (i.e. magnetic colatitide). The polar map shows the distribution of the 20 nearly uniformly spaced sub-beams, some noticeably more intense than others. The nearly tangential character of our sightline traverse is evident from the apparent

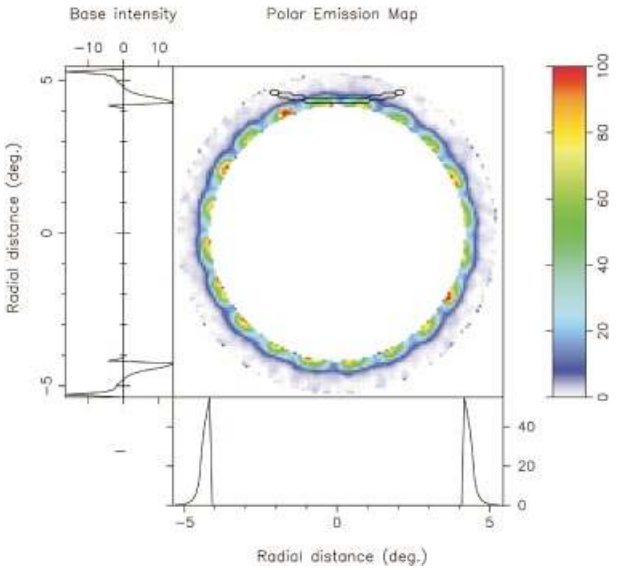

Figure 10. An image of the accessible emission zone reconstructed using the 'cartographic' transform as defined by equations (5)–(8). This image is based on the observed 'B'-mode sequence of 816 pulses. The image or polar map is projected on to the polar cap shown in the main panel, with the 'closer' rotational axis at the top of the diagram. The bottom and the side panels show the average- and the 'base'-intensity profiles, respectively, as functions of the angular distance from the magnetic axis (i.e. magnetic colatitide). Contours indicate the sightline path at the top of the diagram. Here, the star rotates clockwise, causing the sightline to cut the counter-clockwise-rotating sub-beam pattern from left to right.

shapes of the individual features, which are almost certainly depicting only a small outer portion of the 'true' sub-beam structure. The sharply rising radial intensity distribution (bottom panel) and the absence of any hint of a peak (or an inflection) over the accessible range of radii are also indicative of this circumstance.

Note that we have adopted, without loss of generality, a simple but useful convention in this transform, wherein the rotational longitude associated with the magnetic axis defines a vertical line through the image centre, with its top pointing to the 'nearer' rotational pole. So a negative value of β, as in the present case, would correspond to the observer's sightline sampling along a curved track through the upper half of the image. Then the rotation of the star is clockwise when the impact angle β has the same sign as the PA traverse (with respect to the *observed* longitude), and counter-clockwise when it does not. Thus, for the present case, (i) the rotation of the star is in the clockwise direction, and (ii) the sub-beam pattern rotates in the counter-clockwise direction, given that the observed 'drift' is towards the leading edge of the pulse window.

At this point, it is appropriate to ask the obvious question: how unique or even accurate are the results given by this 'cartographic' transformation? The uniqueness – or rather the correctness – of the polar map depends only, and directly, on the correctness of the emission geometry and the other parameters that are required to carry out the transform. It is very sensitive to the circulation time $\hat{P}_3$, the longitude of the magnetic axis φ_0, and the sense of the sightline traverse (i.e. the sign of β) – and if these quantities are incorrect, the image will be smeared or distorted. The actual values of α and β, however, largely just scale the image, so that their correct specification is much less crucial.

In practice, some of these inputs that define the transform may

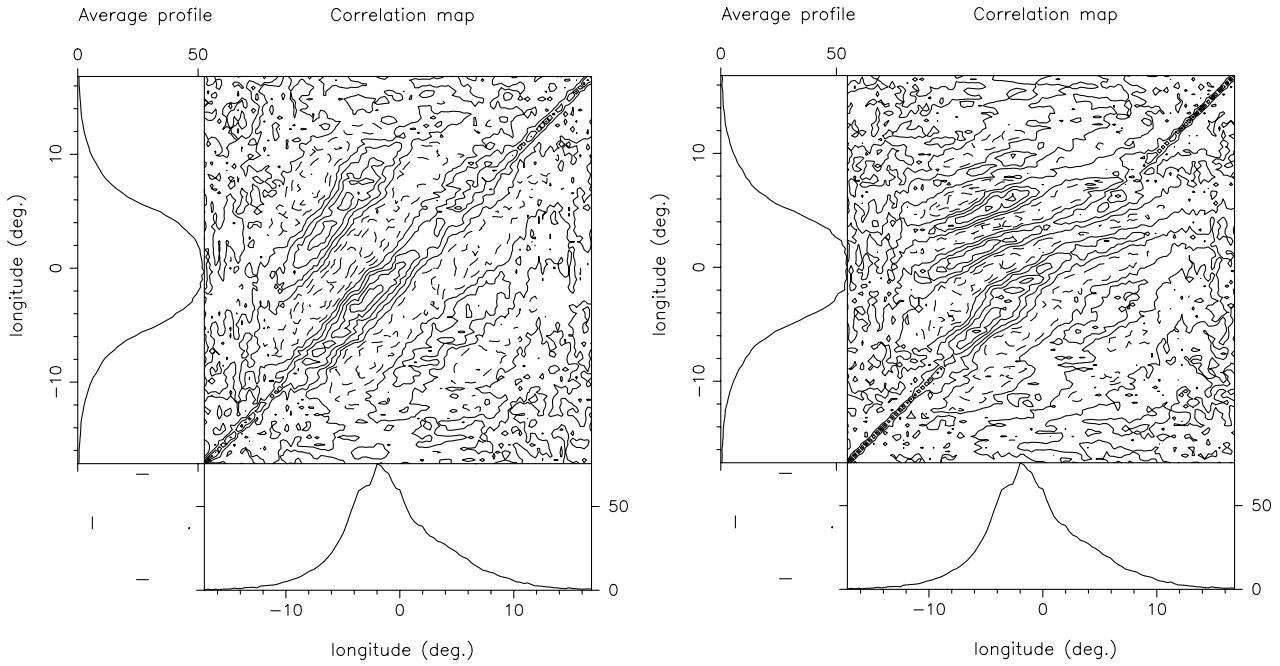

Figure 11. Cross-correlations between the observed pulse sequence and an artificial one computed from the polar map using the inverse 'cartographic' transform. The central panels display the correlation between different longitudes across the pulse window. Two cases are shown which differ only in the sign of the impact angle β, illustrating the usefulness of the inverse transform 'closure path' to assess and refine the geometrical parameters on which the sub-beam imaging depends. The left-hand and bottom panels give the average profiles corresponding to the artificial and the observed sequences, respectively. The contour interval in both plots is about $0.12\,\mathrm{mJy}^2$.

not be known with the desired accuracy, making this transform less conclusive. However, this difficulty can be overcome by invoking an 'inverse' transform, wherein the map reconstructed from the original pulse train is, in turn, used to produce a new sequence of single pulses. If the parameters used in the mapping transformation are indeed correct, then the artificial sequence should match the original one in its detailed fluctuation properties. Comparison of the two sequences is best effected on a longitude-to-longitude basis, such that the new sequence at a given longitude is compared with the original one pulse-for-pulse and sample-for-sample. A simple cross-correlation coefficient, appropriately normalized, provides an adequate quantitative measure for such comparison (although, of course, those for each range of longitude must be combined through a suitably weighted average) – indeed, quite a robust one, given all the possible ways by which the two sequences can differ.

The inverse transform thus provides a powerful 'closure' path to verify and refine the 'input' geometry. The inverse transform, of course, is defined by the same set of relations as for the (forward) 'cartographic' transform. We have used this closure path to confirm our present assumptions and also to rule out conclusively other geometries that were originally considered as plausible.[10] We illustrate this with a simple example of two model geometries, differing only in their sign of β. Shown in Figs 11(a) and (b) are cross-correlation maps of the fluctuations at different longitudes across the pulse window. Plotted in the left and bottom panels are the average profiles for the new and the original sequences, respectively. It is easy to show that the diagonal elements of such correlation maps alone would suffice to assess the match. The other details in the displays do carry important information and can provide useful clues for improving the match.

However, the most significant potential uses of the inverse transform may come through studying what features of the observed sequence are lost in the process of recreating the artificial sequence from the polar-cap map. Note, for instance, that any pattern of sub-beams will produce a sequence that will average to a symmetrical profile – e.g. see the left-hand panels of Fig. 11. These differ noticeably from the asymmetric 430-MHz average profiles observed.

8 THE 'Q'-MODE PULSE SEQUENCE

The 816-pulse sequence thus far considered corresponds to the 'B' mode of the pulsar; this is not the case, however, for the 170 pulses that follow it. Suleymanova et al. (1998) studied the attributes of these two modal sequences, and they find both a sharp boundary between 'B'- and 'Q'-mode characteristics at pulse 816/817 and evidence for slower variations that both anticipate this 'mode change' and follow it. Here, we will first examine the fluctuation properties of this short 'Q'-mode sequence, which is displayed in Fig. 12 – the full sequence, average and pulse-energy variations are given in the main, bottom, and left-hand panels, respectively. We see again that this 'Q'-mode sequence is hardly 'quiescent'; while being weaker overall, some individual sub-pulses are much brighter than any observed in the 'B' mode.

The intensities of this 128-pulse subsequence have been smoothed to reduce the effect of the ultra-strong pulses. Its profile is noticeably broader, particularly on the trailing edge, and its LRF spectra show prominent modulation at an apparent frequency of about 0.23 cycle P_1^{-1}. The HRF spectrum shown in Fig. 13 clearly indicates that the actual modulation frequency is likely to be about 0.77 cycle P_1^{-1}, which would have a first-order alias at 0.23 cycle P_1^{-1} in the LRF spectra.

[10] See Deshpande (1999) for a more detailed discussion of the inverse transform.

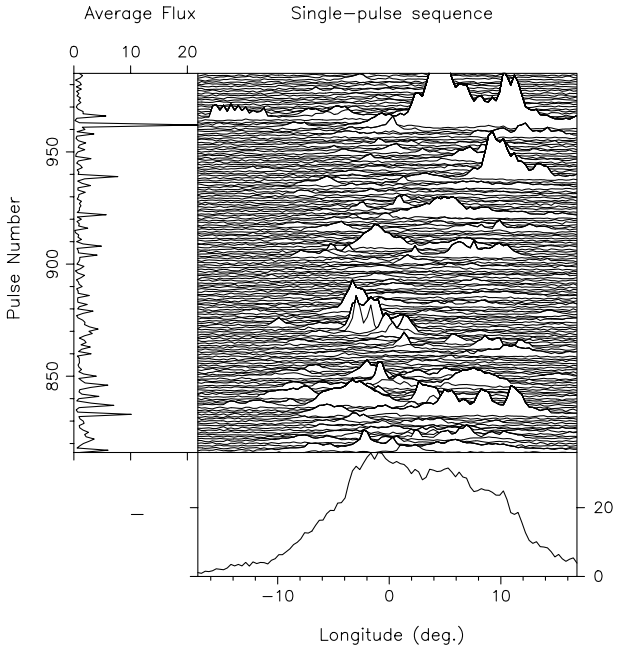

Figure 12. Chaotic individual pulse behaviour during the 1992 'Q'-mode sequence (pulses 817–986). The average profile is shown in the bottom panel and the pulse-energy variation in the left-hand panel. Although the overall emission is weak, the occasional very intense sub-pulses and the enhanced emission on the trailing edge of the window contrast sharply with the 'B' mode.

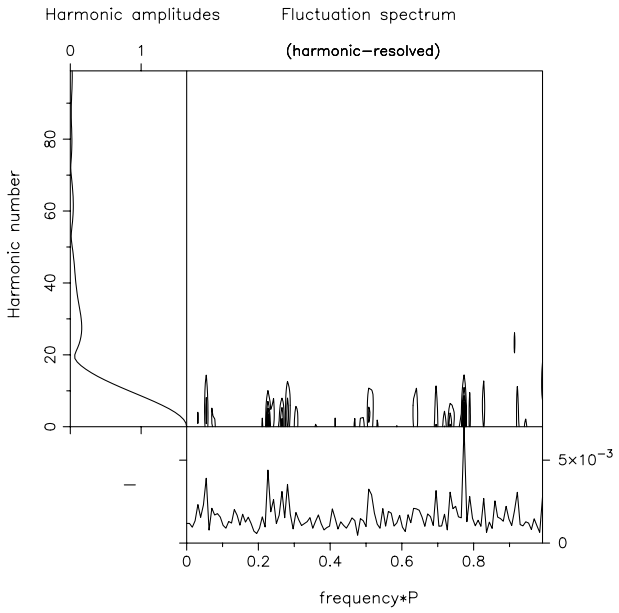

Figure 13. HRF spectrum for the 128-pulse 'Q'-mode sequence as in Fig. 12. The intensities have been smoothed to reduce the dominance of the ultra-strong sub-pulses. The spectrum clearly indicates that the likely true modulation frequency is about 0.77 cycle P_1^{-1}, which would alias to 0.23 cycle P_1^{-1} in the LRF spectra. Contour levels are about 0.015 mJy^2.

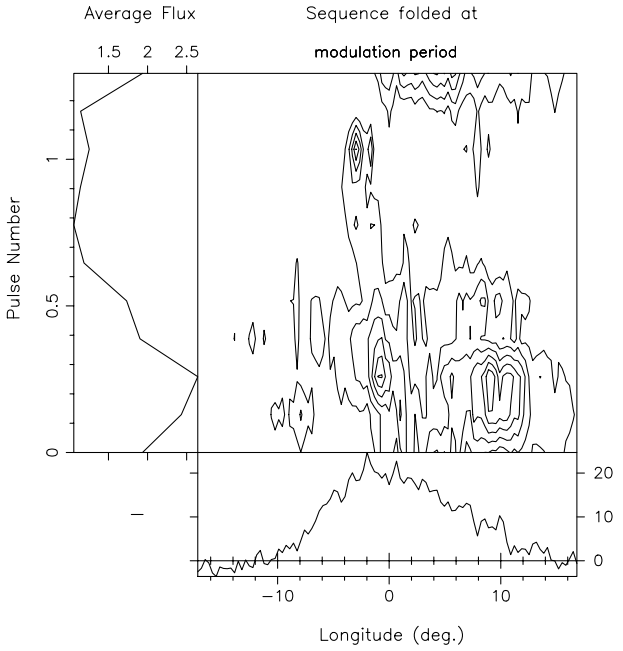

Figure 14. Folded PS corresponding to the 128-pulse 'Q'-mode subsequence in Fig. 12. The data have been averaged over 10 bins spanning the amplitude-modulation feature at $1.293P_1$ cycle^{-1}. The 'base' profile (bottom panel) has been subtracted from the folded sequence (main panel). The modulation is deep and confined to a $-2°$ to $+10°$ longitude range. Contours are at 13-mJy intervals.

Note that the harmonic amplitudes peak at very low numbers – about 1 or 2. If these sidebands are interpreted as a phase modulation, then the corresponding P_2 would definitely be in excess of 180° – that is, it would be larger than the pulse window and comparable to the rotation period. Therefore it cannot be a sub-pulse phase modulation, so we should attribute this feature to amplitude modulation and interpret the asymmetry in the sidebands as resulting from a somewhat faster modulation [with a frequency of 0.77 or 1.77 (2–0.23) cycle P_1^{-1}]. We will assume that the frequency is 0.77 cycle P_1^{-1} and attempt to verify whether this is correct. Fig. 14 shows the sequence as folded at this interval, with the 'base' profile (bottom panel) first subtracted from the main panel display. The modulation is deep and confined to a $-2°$ to 10° longitude interval. We have examined the two halves of this sequence see if the behaviour is similar, finding that the modulation over the wider part of the pulse is common to both subsets (while the feature at about $-3°$ longitude is present only in the first half and thus is probably due to an odd strong pulse). This amplitude modulation feature manifests itself in the pulse-energy variations, where we see a tendency for every fourth pulse to be more intense than the average (see the left-hand panel of Fig. 12).

Apart from this prominent feature, a weak modulation is also visible near (frequency about 5 per cent less than) the primary 'B'-mode feature discussed above, suggesting that the 'B'-mode modulation is not entirely absent. A striking difference between the 'B'- and 'Q'-mode behaviours is the longitude range over which the periodic modulation dominates. Later longitudes are weakly modulated in the 'B' mode, whereas just the opposite occurs here. Moreover, in the one case we see a virtually pure phase modulation, while here we have a strong amplitude modulation. Such marked modulation differences would be more understandable if, for example, the 'Q' mode were

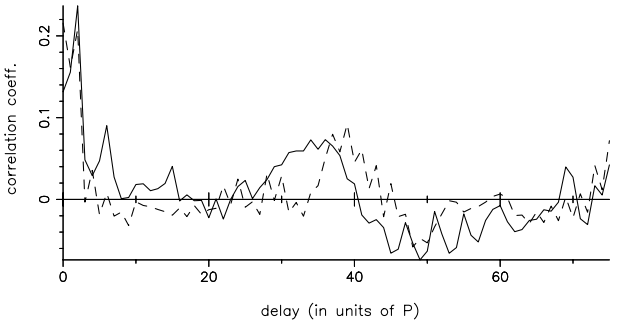

Figure 15. Solid curve: ACF of the 128-pulse 'Q'-mode subsequence shown in Fig. 12. The ACF shown here has been smoothened by a five-lag window to reduce the corrugation contributed by the prominent periodicity discussed above. Dashed curve: results of a similar analysis of 'B'-mode pulses 129–384 for comparison. Note the peaks at a lag of about 40 periods in both cases.

associated with more central longitudes than those of the 'B'-mode, and, while there is some indication that this could be the case, an error in the central longitude could produce much the same effect. Given all these differences as well as the polarization differences, it is surprising that both modes appear to have a nearly identical 'base' profile – where the 'base' is defined as that power which does not participate in the dominant systematic/periodic fluctuations.

The abrupt change in fluctuation features at the 'B'- to 'Q'-mode transition *appears* to begin with pulse 817, which is both broad and very intense. However, the gradual decrease in 'B'-mode intensity that precedes the onset of the 'Q' mode (see Suleymanova et al. 1998) is unlikely to be a coincidence. Hence we have taken a closer look at the behaviour of the sequence just before and after the mode change to see if the ostensibly sudden transition could have been *expected*, or whether it is actually as sudden as it appears. We therefore examined the sequence prior to the 'Q'-mode onset to see if the 0.77 cycle P_1^{-1} feature was present, even at a low level – and, as far as we can determine, it is not.

In an effort to characterize this modal behaviour better, we asked whether the 'cartographic' transform images spanning the 'B'- to 'Q'-mode transition might provide some useful insight. An immediate question to assess, however, was whether or not the parameters defining the transform for the 'B'-mode sequence would be appropriate for the 'Q' mode. Clearly, the geometrical parameters could not change, but we had no a priori means of knowing whether the sub-beam rotation rate would remain fixed. While we were able to determine the round-trip circulation time for the 'B'-mode regime, the 'Q'-mode sequence exhibits no corresponding higher order modulation on which to base an independent determination – as would be the case, for instance, if the sub-beam pattern were not stable over a full rotation. In order to see whether the 'Q'-mode pattern is stable over at least one circulation time, and, if so, to estimate this interval, we examined the autocorrelation function (ACF) of the pulse-energy sequence. The 'Q'-mode ACF (solid curve) shown in Fig. 15 has been smoothed by a five-sample window to reduce the corrugation of the 0.77 cycle P_1^{-1} modulation. For comparison, the dashed curve gives a similar ACF for the 'B'-mode pulses 129–384. The peaks at lags of about 35–40 periods for the 'B'-mode sequence are expected; however, it is remarkable that they appear to persist in the 'Q'-mode sequence as well. Indeed, that both ACFs exhibit

correlation at some 35–40 periods provides very strong evidence that the circulation time of the sub-beam pattern has remained essentially unchanged throughout the transition to the 'Q' mode – despite the dramatic change in modulation properties.

Further, we applied the 'cartographic' transform to a large number of short sequences, each with a large fractional overlap. Viewing the resulting images, in a slow 'movie'-like fashion, allows us to 'see' the evolution of the sub-beam pattern with time.[11] Since each of the images uses a relatively small number of pulses, the sampling is thus somewhat sparse on the periphery of the polar cap. Therefore we have smoothed the image suitably to reduce this patchiness, ensuring that the basic details are not lost. In the early part of the 'B'-mode sequence, most of the 20 sub-beams are bright and nearly uniformly spaced. With time, the individual sub-beams wane and wax in intensity on a scale of several circulation times, and overall they gradually decline in intensity. Some either partially bifurcate or merge with their neighbours, but soon re-establish their characteristic, regularly spaced, vigesimal configuration. Towards the end of the 'B'-mode sequence, most of sub-beams are weak, with only one or two retaining their brightness.

At the onset of the 'Q' mode, most of the sub-beams are weak but still distinguishable; however, first one and then two are exceptionally strong, with their intense discharges filling the area around them and spilling into larger radii or heights. Their lifetimes appear shorter than P_1, not allowing adequate sampling, thus resulting in their 'streaky' character. These dramatic 'Q'-mode events do not entirely displace the old ('B'-mode) sub-beams, some of which crowd together, leaving space in the ring. In the process, more sub-beams appear, the configuration of which is necessarily more compact, which leads to faster fluctuations. Groups of closely spaced sub-beams are evident, with spacings that correspond to the 0.77 cycle P_1^{-1} feature. It would appear that large intervals of weak activity prompt the occurrence of the intense discharges. It may then be that eventually the closely spaced sub-beams evolve so as to have just the right space for 20 – thus re-establishing the characteristic conditions for the bright and stable 'B'-mode configuration.

9 POLARIZATION OF THE SUB-BEAMS

Both our analyses above and those of Suleymanova et al. (1998) raise fundamental questions about sub-beam polarization.

(i) How is the average profile composed of primary polarization mode (PPM), secondary polarization mode (SPM) and perhaps unpolarized (UP) power, and what is the relation between the linear and circular polarization in the former?

(ii) How can we account for the longitude offset between the PPM and SPM partial average profiles?

(iii) Do the two modal profiles have distinct PA sweep rates, and how do these combine in the total 'B'-mode average profile?

(iv) How does the depolarization of the stellar radiation occur, and can we understand it as the incoherent mixing of two fully (but orthogonally) polarized basis modes?

(v) How does the polarization of the rotating-beam system differ from that of the constant 'base' profile?

(vi) What do the polarization 'maps' of the sub-beams tell us about the conditions of their emission?

In order to explore these questions, we have developed several 'mode separation' techniques. Heretofore, such methods have been used to segregate a pulse sequence, sample by sample, into a pair of modal partial profiles (and sometimes a residual profile) (Cordes, Rankin & Backer 1978; Gil et al. 1981; Rankin 1988; Rankin & Rathnasree 1995, 1997),[12] but for our present purposes we require techniques for separating the original sequence into a pair of polarized modal *sequences* (and perhaps an unpolarized sequence). The first method, which we have called 'modal repolarization', assumes that all the observed linear and circular depolarization results from incoherent orthogonal-mode mixing. Under such an assumption, the linear and circular depolarization occurs in strict proportion, as (apart from an overall angle) the linear can also be regarded as simply positive or negative (indeed, as it is represented on the Poincaré sphere). The object is then to restore the observed (depolarized) sequence to a hypothetical pair of fully polarized modal sequences, preserving both the total power and the ellipticity of the original sequence.

In practice these methods proceed by examining the total intensity i and total linear polarization l of the sequence, sample by sample, and then determining whether they respectively fall above or below a threshold $t\sigma_N$, where t is a chosen value (usually taken to be 2.0) and σ_N is the estimated on-pulse rms noise level. If both the quantities are above the threshold, then the observed PA is checked to see whether it falls within $\pm\pi/4$ of the model PA. The detailed mathematics are given in the Appendix. We have tested this 'modal repolarization' method on pulsars for which its motivating assumption is best exemplified – B1929+10 being the canonical such pulsar (Rankin & Rathnasree 1997) – and it functions remarkably well both at modest S/N ratios and when virtually all of the total power is in one of the modes. Of course, we make no claim that these methods are *precisely* correct in a formal statistical sense, but they represent a convenient and useful technique for our purposes.

The sequences of some pulsars cannot so readily be understood as resulting simply from the combination of two fully polarized basis modes, and those of 0943+10 provide one such instance. It appears that a portion of the polarized and unpolarized power in its sequences has a different origin from the rest of the contribution, and so we have also found it useful to divide the original sequence three ways, into two fully polarized modal (PPM and SPM) sequences and a third unpolarized (UP) sequence. The operation of this 'polarization segregation' method is quite similar to the two-sequence 'repolarization' method above, and we both discuss its details in the Appendix and immediately apply it in our analysis and discussion below.

The three panels of Fig. 16 give the respective 'B'-mode average profiles corresponding to the PPM, SPM and UP sequences. The virtually complete, elliptically orthogonal polarization of the modal averages – and the negligible levels of polarization in the latter average – demonstrates the efficacy of our segregation technique. Note that the PPM is about five times greater than the SPM, both in power and in peak intensity, as the effective widths of their respective profiles are about the same ($6\overset{\circ}{.}7$ versus $7\overset{\circ}{.}1$). The PPM profile leads the SPM one by some 3°, and they are slightly left-hand- (LHC) and right-hand-circularly

[11] These 'moving' images can be viewed at web sites with the following URL addresses: http://www.rri.res.in/~desh and http://www.uvm.edu/~jmrankin.

[12] McKinnon & Stinebring (1998) have carried out a very interesting analysis, which also shows that incoherent mode-mixing can account for the depolarization in B2020+28.

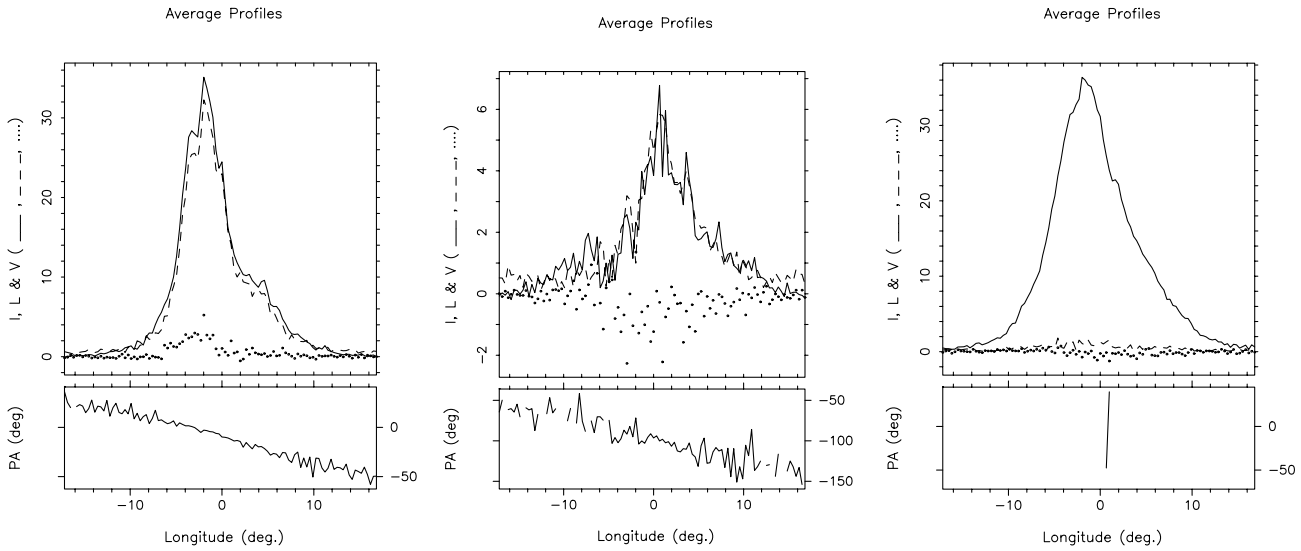

Figure 16. Polarized partial-average profiles corresponding to the PPM, SPM and UP partial sequences, respectively. Note that the PPM and SPM profiles are both highly polarized and elliptically orthogonal. By contrast, the UP profile exhibits a negligible level of polarization. Note also that the PPM and UP sequence averages are comparable, both in power and in mean (scale) intensity, whereas the SPM average is about 5 times weaker. The scales are in mJy.

(RHC) polarized, respectively. Less than half (45 per cent) of the total 'B'-mode power is polarized, but the greater UP profile width (9°.7) makes the modal and UP contributions to the total intensity roughly equal at most longitudes.

The PA traverses of the PPM and SPM in Fig. 16 are, overall, quite linear, but the curves carry little information in the wings of the profiles, where the linear power is low and thus ever more influenced by the choice of the model PA traverse. Suleymanova et al. (1998) found a very significant difference in the PA rates of the 'B'- and 'Q'-mode profiles, and, given that the former is PPM- and the latter SPM-dominated, there is a case to be made. We find it hard to understand, though, how the PPM–SPM difference could be anywhere as large as the 50 per cent (−2°.4 versus −3°.6 per degree) 'B' mode–'Q' mode difference that they find. We have examined PA–frequency maps and the modal partial profiles above, and conclude that the PPM *might* be as flat as −2°.4 per degree and the SPM as steep as −3°.0 per degree, but these seem to be outside limits. Even these small differences in modal PA rate, however, combined with the longitude offset between their power centres, are probably sufficient to explain the peculiar form of the overall PA traverse, which is shallow at negative longitudes and then steepens significantly at positive ones. Note that the rate difference implies that the angle between the two modes will be significantly less than 90° at +10° longitude, just where the overall traverse is steepest.

Turning now to the polarization of the sub-pulse 'drift', the PPM, SPM and UP sequences provide ideal instruments for identifying its characteristics. First, each of these sequences can be folded at the basic $1.87P_1$ phase-modulation cycle (P_3) as we did in Fig. 8 above. Fig. 17 then depicts the behaviour of the PPM- and SPM-associated modulations – the former is given as a set of contours and the latter as a grey-scale. Their relationship is quite striking. We know the slopes of the 'drift' tracks quite accurately; clearly, on average, the sub-pulses move through −10°.5 longitude (P_2) in the $1.867P_1$ cycle, or some $5°.62/P_1$.

We see in Fig. 17 that the PPM and SPM tracks are parallel as expected, although we could not have anticipated that the latter would fall almost exactly in between the former, so that the PPM

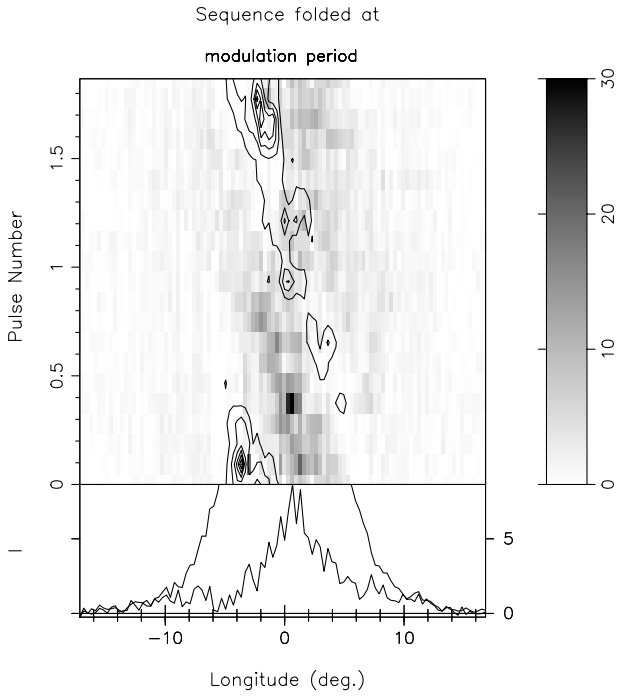

Figure 17. Block-averaged PSs computed from the respective PPM and SPM partial sequences as in Fig. 8 – the former shown as a set of contours and the latter as a grey-scale plot. Note that both PPM and SPM 'drift' along parallel 'tracks', but at somewhat different phases within the overall $1.87P_1$ (P_3) modulation cycle.

and SPM sub-pulse 'tracks' will always be found at a longitude interval of $P_2/2$ or some 5°.3. The overall behaviour is a little more complex, however, because there is a significant phase difference between the PPM and SPM maxima within the phase modulation cycle. Not only does the SPM 'drift'-band maximum lag the PPM one by about $0.25P_1$, but also the respective intensity variations over the cycle appear to be almost reflections of each other – that is, the PPM exhibits a long slow increase and then an

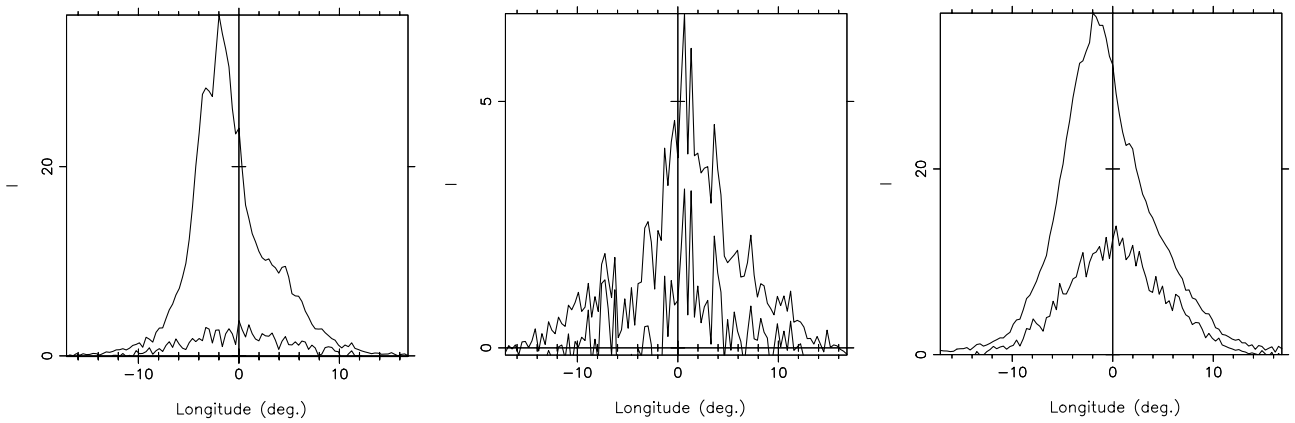

Figure 18. Partial-average profiles for the PPM, SPM and UP partial sequences showing the relative contributions of the aperiodically fluctuating 'base' within each partial sequence. Note that the 'base' comprises a small part of both the PPM and SPM power, but constitutes nearly half of the UP power. Note also that it is quite symmetrical about 0° longitude. The 'base' in each case reflects both the power that is steady from pulse to pulse and any that is fluctuating at a different rate from the phase-modulation rate.

abrupt fall, whereas the SPM cycle appears to begin with a steep increase which then tails off gradually.

In order to examine this behaviour in more detail, Fig. 18 gives the result of folding each of the three partial sequences at the $1.867P_1$ phase-modulation interval. Here we give only the sequence averages (full curves) and the relative amplitude of the 'base' profiles inside them. This 'base' has often been subtracted in displaying the results of our analyses and represents that power which is either constant from pulse to pulse or fluctuating at frequencies other than the phase-modulation rate. One can readily see here that most of the power associated with the PPM and SPM is fluctuating with the basic $1.867P_1$ cycle – and is therefore associated both with the 'drifting' sub-pulses and with the rotating sub-beam system. Much of the UP power is also fluctuating and can be seen largely to follow the PPM 'track' as expected; although nearly half of this power is *not* fluctuating in this way, and thus must have a different origin. It is the sum of these three contributions to the 'unfluctuating' power that we encountered above as the triangular 'base' profile in Fig. 8 – and there questioned whether this power, on account of its $\simeq 11°$ width, could be associated with the weak 'skirt' of a core component.

We have also carried out a similar analysis using the two partial sequences generated by the 'repolarization' technique, and the result is telling. Of course, any depolarization within a sequence can be interpreted as orthogonal mode mixing and the characteristics of the original pair of fully polarized sequences then estimated. For 0943+10, however, the large fraction of the total power that we saw above in the UP sequence is divided equally between the modal sequences in the two-way split and then (because its fluctuations are correlated with those of the PPM) dominates the weaker SPM fluctuating power in its sequence. These circumstances both make this latter technique less useful in the case of 0943+10 and again suggest that some part of the UP power originates from a source other than the mixing of two fully polarized basis modes. This line of interpretation is consistent with the UP being, mostly, a weak signature of core emission, but certainly does not prove that this is the case. Note that the Stokes profile corresponding to this 'base' emission shows only slight linear polarization with a PA following the SPM traverse and a little negative circular polarization.

Of course, each of these partial PSs can also be mapped on to the polar cap using the 'cartographic' transform, and the relation between the PPM and SPM beams is shown in Fig. 19. Here, the PPM emission is shown as a set of contours and that of the SPM as a grey-scale map. The respective intensity scales are, necessarily, not equal; the SPM scale has been enhanced by a factor of about 5 for clarity.

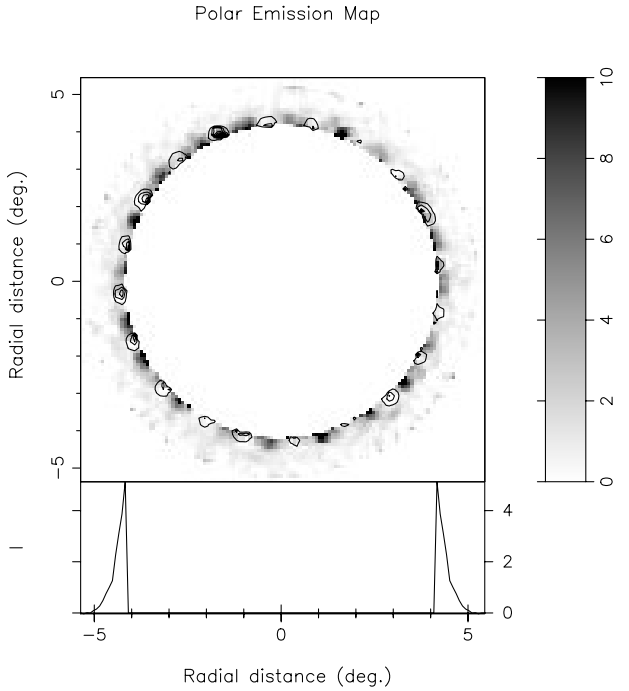

Figure 19. Images of the accessible emission zone as in Fig. 10. The PPM is shown as a set of contours and the SPM as levels of grey. The scales of the two modes are not equal, the weaker SPM having been enhanced so as to be approximately as prominent as the PPM. Note that the SPM power falls between the PPM sub-beams. Recalling that the sub-beam pattern rotates counter-clockwise, and that the rotation of the star sweeps the sightline through the top of the sub-beam system from left to right, we see that the SPM emission generally lags the PPM beams by just less than half the interval between them (see text).

Note, first of all, that the SPM emission also forms a set of sub-beams along nearly the same circle as that of the PPM. Indeed, we know that all these sub-beams rotate counter-clockwise about the magnetic axis at the centre of the diagram and that the overall

clockwise motion of the star about its rotation axis (at the top of the diagram) causes the sightline path to traverse from left to right through the beams, just poleward of the magnetic axis. The different longitude centres and modulation phase of the SPM and PPM power together determine the relative (azimuth) orientation of their respective sub-beam systems. On average, the SPM sub-beams lag their preceding PPM neighbours by an interval which is a little less than half the mean sub-beam spacing. It is just this lag that is reflected in the delay of the SPM profile power centre relative to that of the PPM in Fig. 16. Indeed, we see there that the SPM power centre follows the PPM one by 3°–4° out of the 10°.5 spacing between sub-pulse 'drift' bands (P_2). Note also that both the SPM and PPM beams vary markedly in mean intensity, and there is some correlation between the strength of an SPM beam and that of the PPM beams adjacent to it. Again, on average, the two beam systems both seem truncated at the absolute limit imposed by the sightline traverse – and to about the same extent.

Finally, we can locate the circular polarization within the 'drift' bands and within the sub-beam system in a similar fashion. Fig. 20 again shows the result of folding the sequence at the $1.87P_1$ modulation-cycle interval, but here we see the total power (Stokes I) plotted as a contour map and the circular polarization (Stokes V) given as a colour scale. It is immediately clear that positive (LHC) circular polarization is associated with the total power – which in turn is dominated by the PPM emission; whereas bright negative (RHC) circular polarization is seen along the parallel 'track' corresponding to the SPM. Note that the fractional circular polarization can reach high levels at certain points in the diagram for both modes, but that its average level remains low. Of course, the implied beam configuration of this circular polarization can also be viewed using the 'cartographic' transformation, and Fig. 21 gives this result. Again, the total power is shown as a set of contours and the circular as a colour scale. Here also, we see LHC polarization associated with the PPM beams as well as the region 'outside' them – that is, further from the magnetic axis or perhaps at greater height along the same field lines. Similarly, the RHC is found just between the PPM beams near the positions of the SPM beams in Fig. 19 and also 'outside' them.

Overall, the results of our analysis in this section are quite clear. The rotating sub-beam system that we encountered in earlier sections is highly polarized in an elliptically orthogonal manner: the prominent 20-fold sub-beam system is dominated by PPM emission, which also exhibits systematic LHC polarization. Then, interleaved with this PPM beam system is a similar, weaker SPM beam system which we find to have significant RHC polarization. These circumstances appear to suggest a set of very specific conditions within the emission region, and we will come back to a discussion of their implications later.

10 THE 1972 JANUARY 430-MHz SEQUENCE

In this section, we look at a PS which was recorded at Arecibo in early 1972 (Backer et al. 1975) in order to explore whether the conditions encountered in the 1992 observation are typical or unusual. We have assessed the quality carefully and have selected a subset composed of pulses 201–968 (using only the RHC polarized channel as the other was corrupted by 60-Hz interference) from this old 1000-pulse polarimetric observation. Here, both the single-pulse S/N and resolution are poor relative to the newer sequence – so we used a three-sample smoothing to improve the S/N (at the cost of poorer resolution) but retained the original sampling. Here, too, we find the gradual, monotonic decline in the pulse energy with time, much like what was seen in the newer sequence. The average profile, however, has a more symmetric appearance, which is intrinsic and not a result of the smoothing.

In order to examine the fluctuation properties of the sequence, we computed both the LRF and HRF spectra. The latter is given as Fig. 22, and its dominant spectral feature at 0.5409 ± 0.0009 cycle P_1^{-1} appears in the LRF at 0.46 cycle P_1^{-1} (as a first-order alias as discussed in Section 3). These features correspond to the phase modulation associated with the rotating sub-beams. The second-harmonic feature is not visible in these spectra, but is present when the smoothing is not performed. The harmonic amplitudes of the fluctuation features in the HRF are centred at harmonic numbers 32 and around 65, implying a typical sub-pulse separation of about $11° \pm 0°.5$. The sequence was also folded at the primary modulation period in the manner of Fig. 8 and exhibited a nearly identical behaviour. The 'drift' band was clearly visible, once the 'unchanging' base contribution was removed from that folded over the modulation cycle. The modulation period (P_3) used here corresponds to a refined value $[(1 - 1/2.1755)^{-1}P_1]$ at which the modulation pattern shows maximum contrast in pulse-energy variation across the modulation cycle. Here, there was also a slight suggestion that the sub-beams cross our sightline twice during each complete circuit in magnetic azimuth; if so, it would imply that their angular distance from the magnetic axis is larger than $|\beta|$, which is consistent with many subaverage profiles showing a 'conal double' appearance. Also, since the two crossings through our sightline are generally expected to be symmetric with respect to the 'true' longitude origin, they provide a useful and independent estimate of the central longitude value that we used. The 'base' profile in this subsequence, though, had a larger fractional intensity and a half-power width of about 10°, consistent with the 'base' width in the newer observations.

We also computed the phase variation of the modulation feature (at f_3) as a function of longitude, and the results were virtually identical to Backer et al.'s (1975) fig. 4 (although we have taken care to specify the central longitude correctly). The rate of change of the modulation phase with respect to longitude gives an independent estimate of P_2, which we find encouragingly consistent with that suggested by the HRF spectrum as well as with that found for the 1992 sequence. Based on this similarity, we estimate (using equation 3) the secondary modulation period to be about $20 \times P_3$.

Unfortunately, the relatively noisy character of this sequence has frustrated our efforts to use the intensity ACF to confirm our estimate for the round-trip circulation time. The modulated intensity here is a smaller fraction of the average intensity than in the 1992 observation. Also, there is noticeably more emission at longitudes corresponding to the profile wings (i.e. at outer radii) where the intensity fluctuations are high, but it does not appear to have any definite periodicity. This 'outer' emission is clearly seen in the average-profile 'wings' as a pair of weak, roughly symmetrical features.

We have attempted to map the average sub-beam distribution of this sequence, using a circulation time of $37.014P_1$ and the 'inside, inner' geometry discussed earlier. The central longitude estimate was verified using a bootstrap procedure based on the inverse transform 'closure'. Fig. 23 shows the result after smoothing the map with a circular function having an 8-pixel area to reduce its noisy appearance. The overall character of the distribution is quite similar to that of the 1992 'B'-mode sequence; however, this map shows significant emission at outer radii – probably from an outer

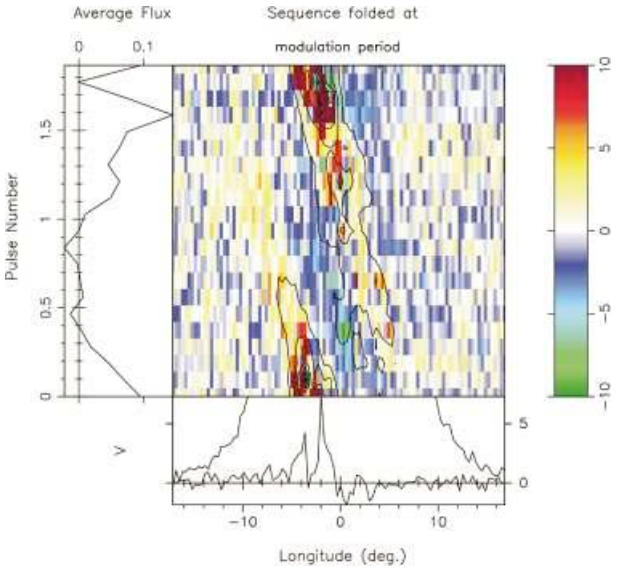

Figure 20. Block-averaged PSs computed from Stokes parameters *I* and *V*, respectively, as in Fig. 8 – the former shown as a set of contours and the latter as a colour plot. Note that the PPM-dominated *I* 'drifts' along a 'track' that has significant LHC polarization, while RHC polarization lies along the adjacent SPM 'track'. The circular polarization can be quite strong at certain positions along these 'tracks', but overall remains at a low level.

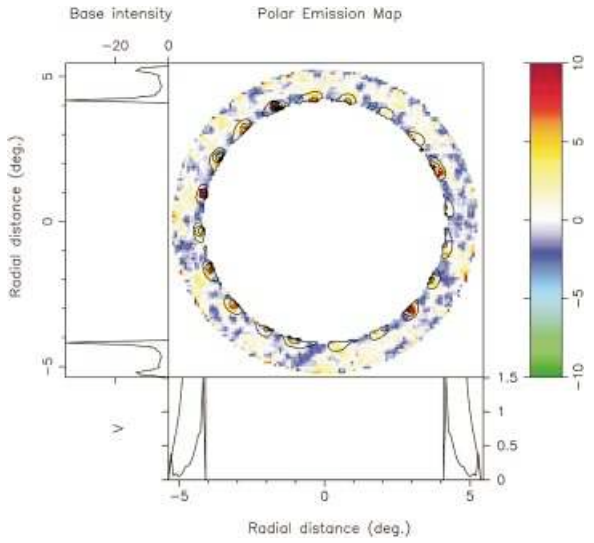

Figure 21. Images of the accessible emission zone as in Fig. 10. Stokes *I* is shown as a set of contours and Stokes *V* as a colour plot. Note that the PPM-dominated *I* sub-beams are LHC-polarized, whereas the SPM-associated region between them is RHC-polarized. Each of these circularly polarized regions has a tendency to extend to 'outside' regions, which may be indicative of higher altitudes in the emission region.

ring of more or less randomly spaced sub-beams. This 'outer' emission is different in kind from that of the 'Q' mode at a similar radius, basically because its distribution is so 'conal' but random in azimuth.

To summarize, this 'old' sequence seems to show all the primary 'B'-mode characteristics, together with some weak and random emission possibly associated with the same sources as the 'Q'-mode emission. The secular decrease in pulse energy may well be an indication of an intense but sporadic 'Q'-mode sequence to follow. The modulation frequency is a little higher than that of the recent observation, but it is well within the variations seen in short sections of the more recent sequence.

11 THE 1990 JANUARY 111.5-MHz SEQUENCE

Now we examine a sequence observed at a longer radio wavelength. It consists of more than 1000 pulses, and we have looked at the first 1024 pulses in detail. At this lower frequency the profile has two well-resolved components separated by about 10° longitude, implying that here the radiation-cone radius ρ is larger than the impact angle $|\beta|$. This is not at all surprising if we are observing emission from the same sub-beams the outer periphery of which we imaged at 430 MHz. We would expect to see them more fully at lower frequency, because of the ever larger emission-cone radius. Indeed, our favoured geometrical model in Table 2 indicates a conal beam radius ρ some 0°.26 larger than at 430 MHz, or, said differently, $|\beta|/\rho$ is here 0.96 as opposed to 1.02 at the higher frequency. This is a major advantage; and we will then hope to 'see' a larger portion of the actual radial extent of the sub-beams.

Let us first examine the fluctuation properties of this sequence. The dominant feature, even at this frequency, is associated with the nearly alternate-pulse modulation that we meet yet again. Over

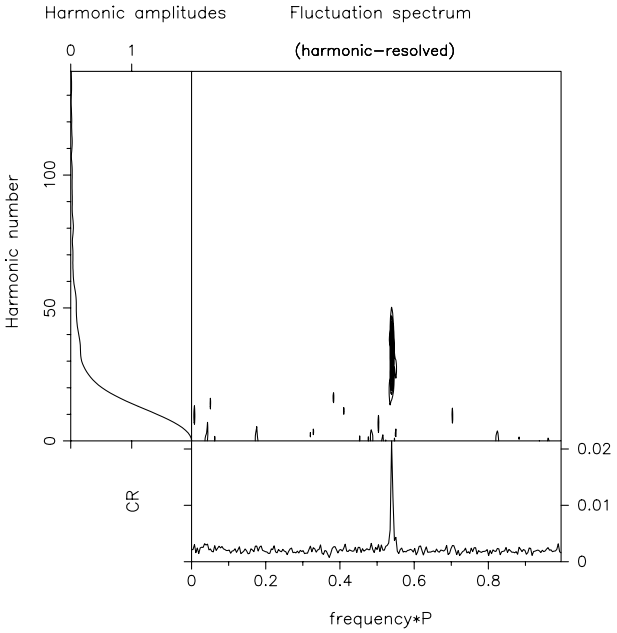

Figure 22. HRF spectrum as in Fig. 4 for the 1972 430-MHz subsequence. Note that the primary modulation feature is at 0.54 cycle P_1^{-1} – related as before to the *aliased* 0.46-cycle P_1^{-1} feature in the LRF spectrum (not shown). Contours are at intervals of 28 mJy^2 up to 198 mJy^2.

the 1024-pulse sequence, the fluctuation frequency varies by perhaps 4 per cent of its mean value, but appears stable over intervals of a few hundred pulses. We show, as a typical example, detailed spectra for pulse numbers 1–350. Other portions of the observation have similar spectra, except for small shifts in the modulation frequency. Fig. 24 shows the LRF spectra, where the aliased feature appears at a frequency of about 0.46 cycle P_1^{-1}. The HRF spectrum (not shown) confirms that the 0.46 cycle P_1^{-1} feature is again the first-order alias of a 0.53 cycle P_1^{-1} modulation

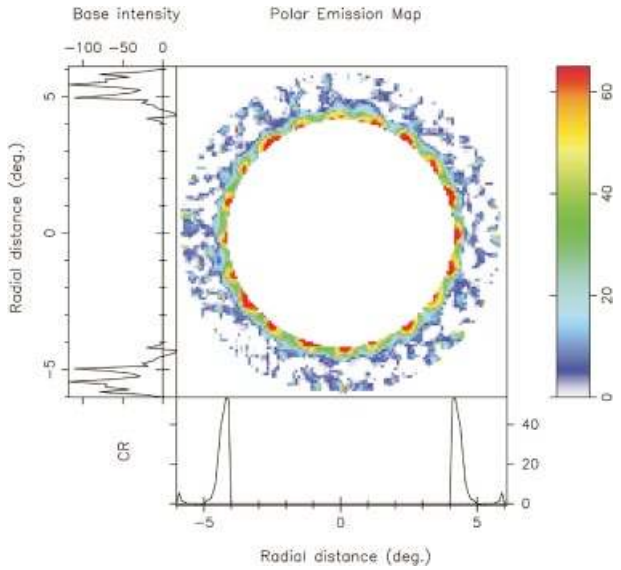

Figure 23. Polar emission map obtained via the 'cartographic' transform for the 1972 430-MHz observation as in Fig. 10. The map is smoothed with a circular 8-pixel-area window to reduce the noise in its peripheral regions.

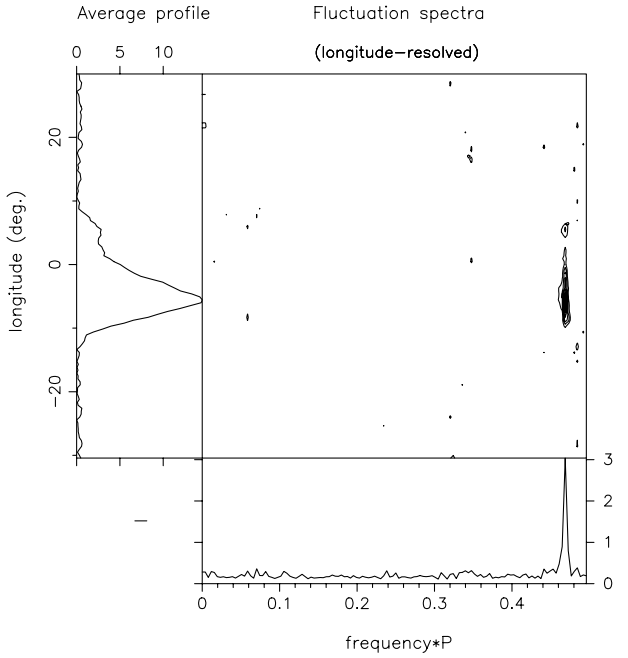

Figure 24. LRF spectra (using 256-point FFTs) for a subsequence (pulses 1–350) of the 1990 111.5-MHz observation (main panel), and the total spectrum (bottom panel) as well as the average profile (left panel). Note the similarity between these spectra and those at 430 MHz. The intensity units are arbitrary.

and that it is phase modulated. Its second harmonic was found close to 0.07 cycle P_1^{-1}. The harmonics related to both the rotational and the phase modulation show a distinctly different envelope compared with their equivalents at 430 MHz. The difference is a direct reflection of the double-resolved profile as against the single form at 430 MHz. The HRF spectrum confirms that the harmonics of the modulation feature peak at about number 32, again implying a P_2 of some 10°–11°.

Next, we look at the result of folding the 350-pulse subsequence at the corresponding modulation period (see Fig. 25). A prominent

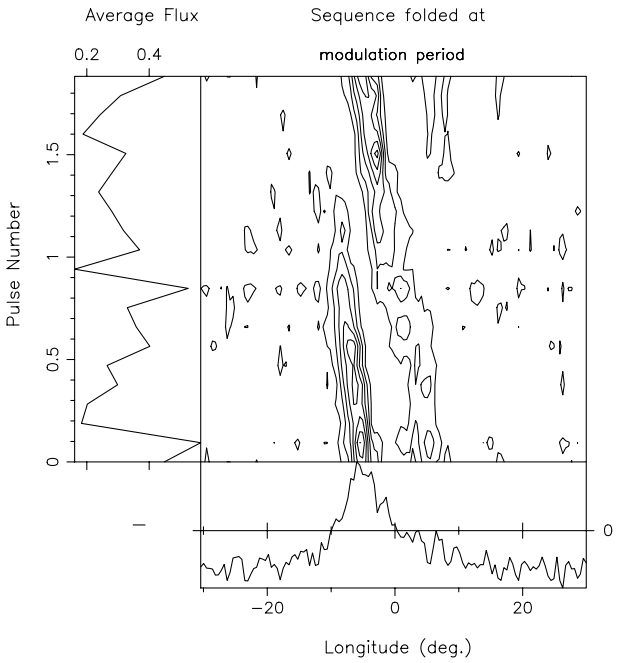

Figure 25. Subsequence folded over the modulation cycle for the same 1990 111.5-MHz observation as in Fig. 24 (main panel); the 'base' profile (bottom panel) has been removed. Note the two distinct tracks associated with the two components seen in the 111.5-MHz average profile. This should be contrasted with the single 'drift' track seen at 430 MHz (see Fig. 8).

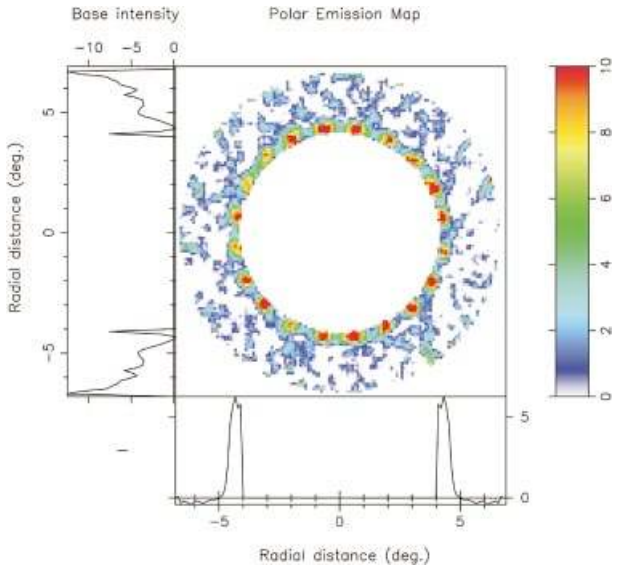

Figure 26. Polar map obtained via the 'cartographic' transform of the same 1990 111.5-MHz subsequence as in Fig. 24 (main panel). The map has been smoothed with a circular (8 pixel area) window to reduce the noise in the peripheral, poorly sampled areas. Note the less elongated appearance of the sub-beam features as compared with those in the 430-MHz maps, implying that the more interior 111-MHz sightline samples the beams more fully. The intensity scales are arbitrary.

'drift' band associated with the leading component is seen in the left half of the main panel. Appearing as a faint continuation is the 'track' associated with the 'drift' of the weaker trailing component. The 'base' profile subtracted from the fluctuations

in the main panel is given in the bottom one. Note that it here resembles the average profile, unlike what we observe at 430 MHz. It is more likely, therefore, that this 'base' reflects aperiodically modulated residual emission, stemming possibly from variations between the 'drift' bands of different sub-beams, rather than being the result of another form of radiation. The variation in the modulation phase (not shown) is remarkably similar to that seen at 430 MHz, implying about the same value of P_2 as determined earlier. The conclusions based on the first set of 350 pulses are seen to be valid throughout the entire sequence, apart from small differences in the modulation frequency. It may be worth recalling that such differences, although on a reduced scale, were also evident in the recent 430-MHz sequence. Such differences can come about as an amplified effect (by a factor of $360^\circ/P_2$) of possible tiny fractional changes in sub-beam spacing, rather than direct changes in the circulation rate.

We now proceed to perform the 'cartographic' transformation. Having noted that the modulation properties are nearly identical to those for the 430-MHz 'B'-mode sequence, the conclusion that the round-trip delay is quite close to 20 times the mean P_3 is unavoidable. However, since the differences in the P_3-values for the various sections of this PS are found to be different by more than the available resolution in P_3 (which is simply the inverse of the number of pulses in the sequence), we should perform the transform on suitable sections of the data separately, unless we wish to view only the average distribution of the sub-beams. With the geometry already defined, we use the different subsequences and the inverse-transform 'closure' to confirm our estimate of the central longitude, and then examine the sub-beam distributions (in simple projection on to the polar cap) for the different sections separately. Fig. 26 shows one such map, again corresponding to the first 350 pulses. The other subsequences show a similar distribution of sub-beams, differing only in their detailed intensities and the locations of individual sub-beams. As anticipated, we now see a much larger fraction of each of the sub-beams than was possible at 430 MHz. The radial profile (in the bottom panel) shows an intensity maximum well outside the β cut-off. In fact, the portion of the sub-beams invisible now is comparable to that visible at 430 MHz. By comparing the radial profiles at the two frequencies, we can now estimate the factor by which the radiation-cone size has changed: 1.03 between 430 and 111.5 MHz, which is in good agreement with the modelling in Table 2.

12 SUMMARY AND CONCLUSIONS

In this first paper of a series, we develop techniques and present detailed studies of the 'drifting' sub-pulses of pulsar B0943+10, based on three sets of Arecibo observations. Pulse sequences from this star are remarkable for their extraordinary stability and apparent complete lack of null pulses. Future papers in this series will feature sequences of several different kinds from other low-frequency observatories, as well as overall analysis and physical interpretation of their significance.

Our main results can be summarized as follows.

(i) We have resolved the question of whether the primary spectral feature of 0943+10 is aliased and whether the secondary feature is its second harmonic. The primary feature at about 0.46 cycle P_1^{-1} is the first-order alias of the fundamental phase modulation, which has a true frequency of about 0.53 cycle P_1^{-1}. The secondary feature is then indeed a second harmonic (at about 1.07 cycle P_1^{-1}), which is seen as a second-order alias at about 0.07 cycle P_1^{-1}.

(ii) Three new techniques have been developed and applied to resolve the above questions. (a) A 'harmonic resolved fluctuation' spectrum uses the information within the finite width of the pulse to achieve a Nyquist frequency of 1 cycle P_1^{-1}, showing clearly that the primary feature is aliased. Then, the harmonicities of both (b) the harmonic amplitudes of the two features and (c) their phase rates are used to argue that the former appears as a first-order alias and the latter as a second-order one.

(iii) Using several different techniques, we have been able to measure the longitude interval between adjacent sub-pulses P_2, as well as the PA rotation corresponding to this interval χ_{P_2}, and to relate these to the azimuthal angle η between adjacent sub-beams around the magnetic axis of the star. The most reliable values of P_2 come from either the principal harmonic number of the phase modulation or the phase rate associated with its primary feature, both of which yield values of about $10\overset{\circ}{.}5 \pm 0\overset{\circ}{.}5$. Interestingly, we find that $|\chi_{P_2}|$, which just less than 30°, should exceed P_2 for an inner sightline traverse, and vice versa; and that η is approximately the difference between these quantities. Thus η must be near 18° for 0943+10, implying a system of some 20 sub-beams.

(iv) A pair of 'sideband' features are observed in the overall fluctuation spectra (and very strongly in certain sections). We identified these features as an amplitude modulation on the primary phase modulation. Such features can only occur if this tertiary amplitude modulation is stable and harmonically commensurate with the primary phase modulation. The separation between the 'sidebands' and the primary feature Δf is just 1/20 of the 0.54 cycle P_1^{-1} frequency, indicating that the tertiary modulation is produced by a repeating pattern of just 20 elements. The overall modulation period is then 20 times P_3 or just over $37P_1$, which is dramatically demonstrated by folding the entire sequence at this interval. It is at this point that we have conclusive evidence that the aliasing question is resolved, because $0.5355/\Delta f$ is an integer within its errors, whereas other possible alias frequencies of the primary phase modulation are not.

(v) On this basis, we have been able to determine that P_3 is some $1/(0.53 \text{ cycle } P_1^{-1})$ or $1.87P_1$ and to demonstrate this circumstance by folding the entire sequences at this interval. This implies that that 'drift' is *negative*, or in the same direction as the rotation of the star.

(vi) The 'drifting' sub-pulse pattern of pulsar 0943+10 can be completely understood as resulting from a system of 20 sub-beams rotating around its magnetic axis in an interval of some 37 rotation periods or about 41 s, where some of the sub-beams are stronger than others and maintain this intensity difference for several circulation times.

(vii) We have developed a new technique, involving a 'cartographic' transform and its inverse, to map and study the underlying sub-beam pattern. The forward transform merely expresses the observed pulse sequence in terms of a pulsar-frame magnetic colatitude and azimuth, rotating at the sub-beam circulation rate, rather than the usual parameters of pulse number and phase (or longitude). Techniques are described whereby the forward transform can be used to study and display the sequence, whereas the inverse transform can be applied in a 'search' mode to determine the geometry or other poorly known parameters of the sequence.

(viii) All the techniques including the 'cartographic' transforms have been applied to three different Arecibo observations, two at 430 MHz from 1992 and 1972, and one at 111 MHz from 1990, and entirely compatible results have been obtained for each.

(ix) The polarization characteristics of the most recent

observation have also been carefully investigated. Using new methods of segregating the observed sequences into two or three subsequences with definite polarization states, we have mapped the emission of the pulsar in the two polarization modes and plotted their characteristics. The PPM is about five times stronger than the SPM, and both closely follow a Radhakrishnan & Cooke behaviour at every longitude across the profile[13] – although they appear to have slightly different PA sweep rates. Positive circular polarization is associated with the PPM and negative with the SPM. A part of the unpolarized power, that which 'drifts', seems to be the result of modal depolarization, but another part seems to have an independent origin.

(x) Polarized maps of the beam configuration show clearly that the PPM emission consists of a 20-fold system of bright, well confined sub-beams, whereas the SPM emission is observed as a series of 'beams' interleaved between the PPM system as well as at larger radii (or heights). This and other features of the beam configuration suggest that the pulsar radiates at various altitudes within a system of emission columns generated by a 'seed' pattern at their 'feet'.

(xi) Our qualitative result that the 'drifting' sub-pulse emission of the pulsar is produced by a rotating sub-beam system, as well as our quantitative values for both the circulation time and physical sub-beam spacing (see also Deshpande & Rankin 1999), appears fully compatible with the Ruderman & Sutherland (1975) model, although our analysis is completely independent of this model.

(xii) The methods of the present analysis should be useful for studying the origin of pulse modulation in other pulsars.

ACKNOWLEDGMENTS

We are grateful to V. Radhakrishnan, Rajaram Nityananda and Mark McKinnon for many insightful comments and criticisms on our analysis. We also thank the following people: Svetlana Suleymanova for drawing our attention to this pulsar; Jonathan Arons, Alice Harding, Vinod Krishan, R. Ramachandran and Malvin Ruderman for highly informative discussions; P. Ramadurai for his generous assistance with computing; N. Rathnasree, Vera Izvekova, Svetlana Suleymanova, Kyriaki Xilouris and Amy Carlow for help with the 1992 observing; and Phil Perillat for his Arecibo 40-MHz Correlator software. We each acknowledge the hospitality of each other's institutes, where much of this work was carried out. This work was supported in part by grants from the US NSF (AST 89-17722, INT 93-21974 and AST 99-86754). Arecibo Observatory is operated by Cornell University under contract to the US NSF.

REFERENCES

Backer D. C., 1970a, Nat, 227, 692
Backer D. C., 1970b, Nat, 228, 42
Backer D. C., 1970c, Nat, 228, 1297
Backer D. C., 1971, PhD thesis, Cornell University
Backer D. C., 1973, ApJ, 182, 245
Backer D. C., Rankin J. M., Campbell D. B., 1975, ApJ, 197, 481
Blaskiewicz M., Cordes J. M., Wasserman I., 1991, ApJ, 370, 643
Cole T. W., 1970, Nat, 227, 788
Comella J. M., 1971, PhD thesis, Cornell University
Cordes J. M., Rankin J. M., Backer D. C., 1978, ApJ, 223, 961
Deshpande A. A., 1999, in Kramer M., Wex N., Wielebinski R., eds, ASP Conf. Ser. Vol. 202, Proc. IAU Colloq. 177. Astron. Soc. Pac., San Francisco, p. 149
Deshpande A. A., Radhakrishnan V., 1992, JA&A, 13, 15
Deshpande A. A., Rankin J. M., 1999, ApJ, 524, 1008
Drake F. D., Craft H. D. E., 1968, Nat, 220, 231
Everett J. E., Weisberg J. M., 2000, ApJ, preprint,
Ferraro V. C. A., Plumpton C., 1966, Magneto-Fluid Mechanics. Oxford Univ. Press, London, p. 23
Gil J. A., 1981, Acta Phys. Pol., B12, 1081
Gil J. A., 1992, A&A, 256, 495
Gil J. A., Lyne A. G., Rankin J. M., Snakowski J. K., Stinebring D. R., 1981, A&A, 255, 181
Gil J. A., Kijak J., Seiradakis J. H., 1993, A&A, 272, 268
Izvekova V. A., Kuz'min A. D., Malofeev V. M., Shitov Yu. P., 1981, Ap&SS, 78, 45
Komesaroff M. M., 1970, Nat, 225, 612
Kramer M., Wielebinski R., Jessner A., Gil J. A., Seiradakis J. A., 1994, A&AS, 107, 515
Lang K. R., 1969, ApJ, 158, L175
Lovelace R. V. E., Craft H. D. E., 1968, Nat, 220, 875
McKinnon M. M., Stinebring D. R., 1998, ApJ, 502, 883
Mitra D., Deshpande A. A., 1999, A&A, 346, 906
Narayan R., Vivekanand M., 1982, A&A, 113, L3
Radhakrishnan V., Cooke D. J., 1969, Astrophys. Lett., 3, 225
Rankin J. M., 1988, ApJ, 325, 314
Rankin J. M., 1990, ApJ, 352, 247
Rankin J. M., 1993a, ApJ, 405, 285
Rankin J. M., 1993b, ApJS, 85, 145
Rankin J. M., Deshpande A. A., 1999, in Kramer M., Wex N., Wielebinski R., eds, ASP Conf. Ser. Vol. 202, Proc. IAU Colloq. 177. Astron. Soc. Pac., San Francisco, p. 155
Rankin J. M., Rathnasree N., 1995, JA&A, 16, 327
Rankin J. M., Rathnasree N., 1997, JA&A, 18, 91
Ruderman M. A., 1972, ARA&A, 10, 427
Ruderman M. A., 1976, ApJ, 203, 206
Ruderman M. A., Sutherland P. G., 1975, ApJ, 196, 51
Sieber W., Oster L., 1975, A&A, 38, 325
Slee O. B., Mulhall P. S., 1970, Proc. Astron. Soc. Aust., 1, 322
Suleymanova S. A., Izvekova V. A., 1984, SvA, 28, 53
Suleymanova S. A., Izvekova V. A., Rankin J. M., Rathnasree N., 1998, JA&A, 19, 1
Sutton J. M., Staelin D. H., Price R. M., Weimer R., 1970, ApJ, 159, L89
Taylor J. H., Huguenin G. R., 1971, ApJ, 167, 273
Taylor J. H., Jura M., Huguenin G. R., 1969, Nat, 223, 797
Taylor J. H., Huguenin G. R., Hirsch R. M., Manchester R. N., 1971, Astrophys. Lett., 9, 205
Thorsett S., 1991, ApJ, 377, 263
Vitkevich V. V., Alexseev Yu. I., Zhuravlev Yu. P., 1969, Nat, 224, 49
Weisberg J. M. et al., 1999, ApJS, 121, 171

[13] We see no evidence of the anomalous PA rotation within the 'drifting' sub-pulses as has been reported for 0809+74 by Taylor et al. (1971) and for 2303+30 by Gil (1992).

APPENDIX A: POLARIZATION-MODAL ANALYSIS TECHNIQUES

Here we give the mathematical details of the polarization-mode separation techniques which we used in Section 9. As these techniques proceed sample by sample, we are always concerned with the polarization state of each individual sample, which can be represented by Stokes vector $\boldsymbol{s} = (i, q, u, v)$ in relation to the standard deviation of all sources of noise in any one Stokes parameter σ. The total polarized power p is then $\sqrt{q^2 + u^2 + v^2}$, and the linear power l is $\sqrt{q^2 + u^2}$, where $\chi = \frac{1}{2}\tan^{-1}(u/q)$ is the sample PA. Both techniques require a model PA traverse, which is usually taken to describe the primary polarization mode (PPM) and which, for the sample in question, has a value $\chi_{\rm m}$.

Our modal 'repolarization' technique follows that outlined for

Table A1. The two-sequence 'repolarization' technique.

$l \geq 2\sigma$ and $p \leq i$	$l \geq 2\sigma$ and $p > i$
(partial polarization)	(hyperpolarization)
$s_{\mathrm{p(s)}} = (p', q', u', v')$	$s_{\mathrm{p(s)}} = (i, q, u, v)$
$s_{\mathrm{s(p)}} = (p'', q'', u'', v'')$	$s_{\mathrm{s(p)}} = (\hat{n}, \hat{n}, \hat{n}, \hat{n})$
For $\lvert\chi - \chi_{\mathrm{m}}\rvert < \frac{\pi}{4} \left(\geq \frac{\pi}{4}\right)$	For $\lvert\chi - \chi_{\mathrm{m}}\rvert < \frac{\pi}{4} \left(\mathrm{e} \geq \frac{\pi}{4}\right)$
$l < 2\sigma$ and $i > 2\sigma$	$l < 2\sigma$ and $i < 2\sigma$
(depolarization)	(noise)
$s_{\mathrm{p}} = (i/2, q^*/2, u^*/2, v/2)$	$s_{\mathrm{p}} = (i/2, q/2, u/2, v/2)$
$s_{\mathrm{s}} = (i/2, -q^*/2, -u^*/2, v/2)$	$s_{\mathrm{s}} = (i/2, q/2, u/2, v/2)$

Table A2. The three-sequence polarization segregation method.

$l \geq 2\sigma$ and $p \leq i$	$l \geq 2\sigma$ and $p > i$
(partial polarization)	(hyperpolarization)
$s_{\mathrm{p(s)}} = (p, q, u, v)$	$s_{\mathrm{p(s)}} = (i, q, u, v)$
$s_{\mathrm{s(p)}} = (\hat{n}, \hat{n}, \hat{n}, \hat{n})$	$s_{\mathrm{s(p)}} = (\hat{n}, \hat{n}, \hat{n}, \hat{n})$
$s_{\mathrm{u}} = (i - p, \hat{n}, \hat{n}, \hat{n})$	$s_{\mathrm{u}} = (\hat{n}, \hat{n}, \hat{n}, \hat{n})$
For $\lvert\chi - \chi_{\mathrm{m}}\rvert < \frac{\pi}{4} \left(\geq \frac{\pi}{4}\right)$	For $\lvert\chi - \chi_{\mathrm{m}}\rvert < \frac{\pi}{4} \left(\geq \frac{\pi}{4}\right)$
$l < 2\sigma$ and $i > 2\sigma$	$l < 2\sigma$ and $i < 2\sigma$
(depolarization)	(noise)
$s_{\mathrm{p}}, s_{\mathrm{s}} = (\hat{n}, \hat{n}, \hat{n}, \hat{n})$	$s_{\mathrm{p}}, s_{\mathrm{s}} = (i/3, q/3, u/3, v/3)$
$s_{\mathrm{u}} = (i, q, u, v)$	$s_{\mathrm{u}} = (\hat{n}, \hat{n}, \hat{n}, \hat{n})$

profile polarization by Rankin & Rathnasree (1997); however, we here apply it to the individual samples of a pulse sequence. To this end we require a few more definitions. The total fractional polarization $f = p/i$, so for the primary mode $l' = l/f$ and $v' = v/f$. Then, for the secondary mode, $l'' = -(l' - l)/2$ and $v'' = -(v' - v)/2$. Since the two modes are fully polarized by assumption, $i' = \sqrt{l'^2 + v'^2}$ and $i'' = \sqrt{l''^2 + v''^2}$. Finally, $q' = l' \cos 2\chi$ and $u' = l' \sin 2\chi$, just as $q'' = l'' \cos 2\chi$ and $u'' = l'' \sin 2\chi$.

Insignificant portions of the resulting sequences must be noise-like, just as are the natural ones. Therefore, $\hat{n}$ here represents a noise source – that is, a Gaussian-distributed random variable with zero mean and a standard deviation equal to $\sigma/2$. In generating the two repolarized modal sequences, four different computations are carried out depending upon whether the sample falls above or below two different thresholds, one pertaining to its total intensity relative to the noise level σ and a second to determine whether it is significantly linearly polarized. Only when a sample has significant power but negligible polarization is the model angle used to reconstruct the modes; then we compute the necessary linear $l^* = \sqrt{i^2 - v^2}$ and so $q^* = l^* \cos 2\chi_{\mathrm{m}}$ and $u^* = l^* \sin 2\chi_{\mathrm{m}}$. The overall procedure is then as outlined in Table A1.

The three-sequence polarization segregation method is slightly simpler to carry out. The same thresholds are used, $\hat{n}$ is defined as $\sigma/3$, and the overall procedure is as given in Table A2.

This paper has been typeset from a TEX/LATEX file prepared by the author.